*Clays and Clay Minerals*, Vol. 63, No. 5, 378–394, 2015.

# THE ILLITE–ALUMINOCELADONITE SERIES: DISTINGUISHING FEATURES AND IDENTIFICATION CRITERIA FROM X-RAY DIFFRACTION AND INFRARED SPECTROSCOPY DATA

BELLA B. ZVIAGINA[1,*], VICTOR A. DRITS[1], JAN ŚRODOŃ[2], DOUGLAS K. MCCARTY[3], AND OLGA V. DORZHIEVA[1,4]

[1] Geological Institute of the Russian Academy of Science, Pyzhevsky per. 7, 119017 Moscow, Russia
[2] Institute of Geological Sciences, Polish Academy of Sciences – Research Centre in Krakow, ul. Senacka 1, 31-002 Krakow, Poland
[3] Chevron ETC, 3901 Briarpark, Houston, TX 77063 USA
[4] Institute of Ore Deposits, Petrography, Mineralogy, and Geochemistry of the Russian Academy of Science, Staromonetny per. 35, 119017 Moscow, Russia

**Abstract**—Al-rich K-dioctahedral 1*M* and 1*Md* micas are abundant in sedimentary rocks and form a continuous compositional series from (Mg,Fe)-poor illite to aluminoceladonite through Mg-rich illite. The complexity and heterogeneity of chemical composition and structural features, as well as the lack of reliable diagnostic criteria, complicate the identification of these mica varieties. The objectives of the present study were to reveal the structural and crystal-chemical variability in the illite–aluminoceladonite series, and to define the composition ranges and identification criteria for the mica varieties in the series. A collection of illite and aluminoceladonite samples of various compositions was studied by X-ray diffraction (XRD) and Fourier-transform infrared (FTIR) spectroscopy. Analysis of the relationships between unit-cell parameters and cation composition showed that the series includes three groups, (Mg,Fe)-poor illites, Mg-rich illites, and aluminoceladonites, each characterized by a unique combination of unit-cell parameter variation ranges. The distinctive features of aluminoceladonite are reduced values of $c\sin\beta$ and $|c\cos\beta/a|$ in combination with $b$ parameters that are smaller than those for Mg-rich illites, and slightly greater than those of (Mg,Fe)-poor illites. The compositional boundary between illite and aluminoceladonite occurs at Si = ~3.7 and Mg + $Fe^{2+}$ = ~0.6 atoms per $O_{10}(OH)_2$.

A new approach to the interpretation of the FTIR spectroscopy data involving new relationships between band positons and cation composition of (Mg,Fe)-poor illites, Mg-rich illites, and aluminoceladonites provides additional diagnostic features that include the band positions and profile in the regions of Si–O bending, Si–O stretching, and OH-stretching vibrations. A sharp maximum from the AlOHMg stretching vibration at ~3600 $cm^{-1}$, the presence of a MgOHMg stretching vibration at 3583–3585 $cm^{-1}$, as well as characteristic band positions in the Si–O bending (435–439, 468–472, and 509–520 $cm^{-1}$) and stretching regions (985–1012 and 1090–1112 $cm^{-1}$), are typical of aluminoceladonite.

**Key Words**—Aluminoceladonite, Dioctahedral Mica, FTIR Spectroscopy, Illite, Unit-cell Parameters, X-ray Diffraction.

## INTRODUCTION

A characteristic feature of micas in general and K-dioctahedral micas in particular is a wide diversity of isomorphous cation substitutions in both tetrahedral and octahedral sheets. One of the compositional series conventionally distinguished in K-dioctahedral micas is the solid solution from muscovite, $KAl_2(Si_3Al)O_{10}(OH)_2$, to aluminoceladonite, $KAl(Mg,Fe)Si_4O_{10}(OH)_2$. High- and low-temperature K-dioctahedral micas differ in their ranges of compositional variations. High-temperature Al-rich dioctahedral $2M_1$ and $3T$ true K-micas form a series from muscovite to phengite, $KAl_{1.5}Mg_{0.5}(Si_{3.5}Al_{0.5})O_{10}(OH)_2$, only (Bailey, 1984; Brigatti and Guggenheim, 2002; Ferraris and Ivaldi, 2002). The varieties having aluminoceladonite cation compositions were only synthesized at extremely high temperatures and pressures (Smyth *et al.*, 2000; Schmidt *et al.*, 2001). In a few instances, samples with a phengite-like composition (*e.g.* Ripp *et al.*, 2009; Beyer *et al.*, 2010) were referred to as aluminoceladonites, probably because a certain ambiguity and controversy persist in the nomenclature of micas.

In contrast, low-temperature Al-rich K-dioctahedral micas, which normally occur as 1*M* and 1*Md* polytypes, form a continuous series from illite to aluminoceladonite (Środoń and Eberl, 1984; Drits and Kossovskaya, 1991; Brigatti and Guggenheim, 2002; Drits *et al.*, 2006, 2010a; Wilson, 2013). The IMA Mica Subcommittee proposed the following idealized formula and octahedral compositional range for illite (no tetrahedral compositional range has been proposed):

* E-mail address of corresponding author:
zbella2001@yahoo.com
DOI: 10.1346/CCMN.2015.0630504

$K_{0.65+x}[(Al,Fe^{3+})_{2-x}(Mg,Fe^{2+})_x]_{2.0}(Si_{3.35}Al_{0.65})\ O_{10}(OH)_2$; $^{VI}R^{2+}/(^{VI}R^{2+} + {}^{VI}R^{3+}) \leqslant 0.25$; $^{VI}Al/(^{VI}Al + {}^{VI}Fe^{3+}) \geqslant 0.6$ (modified from Rieder *et al.*, 1998).

This formula and composition range do not cover adequately the complexity and heterogeneity of illite chemical composition. Generally, illites have either a muscovite-like or phengite-like composition, with the layer charge always <1.0 per $O_{10}(OH)_2$ and a lower K content than either in muscovite or phengite (Wilson, 2013). For example, the range of cation compositions for illite structural formulae provided by Środoń and Eberl (1984), Drits *et al.* (2010a), and Wilson (2013) (18 samples) is Si = 3.13–3.62, $^{VI}Al$ = 1.35–1.96, $R^{2+}$ = 0.05–0.62, and K = 0.60–0.84 cations per half-formula unit (p.h.f.u.). The IMA Mica Subcommittee (Rieder *et al.*, 1998) does not encourage the use of descriptive attributes with mineral series names such as illite, glauconite *etc.* In practice, using such attributes is difficult to avoid because of the diverse compositional variations in interlayer-deficient mica varieties, and illite in particular. Following Drits *et al.* (2010a), the term (Mg,Fe)-poor illite will be used here for illite with muscovite-like composition and Mg-rich illite for those with a composition approaching phengitic.

Aluminoceladonite was defined as a true mica having the idealized formula $K[(Al,Fe^{3+})_1(Mg,Fe^{2+})_1]Si_4O_{10}(OH)_2$ and the following octahedral cation compositional range: $^{VI}R^{2+}/(^{VI}R^{2+} + {}^{VI}R^{3+}) \geqslant 0.25$; $^{VI}A1/(^{VI}A1 + {}^{VI}Fe^{3+})$: 0.5–1.0; and $Mg/(Mg + {}^{VI}Fe^{2+}) > 0.5$ (Rieder *et al.*, 1998). No compositional range was proposed for the tetrahedral sheet, which introduces ambiguity in the distinction between aluminoceladonite and phengite or Mg-rich illite. Moreover, in most natural samples of aluminoceladonite or aluminoceladonite-like composition, the interlayer charge is <0.85 per $O_{10}(OH)_2$, which is the minimum value for true micas as recommended by Rieder *et al.* (1998). All these samples are *trans*-vacant (*tv*) 1*M* polytypes that formed at relatively low temperatures and pressures, mostly under the influence of highly-mineralized solutions in evaporite basins (Sokolova *et al.*, 1976; Rasskazov, 1984; Seifert, 1968; Drits and Kossovskaya, 1991; Petrova and Amarjargal. 1996; Murao *et al.*, 2009; Drits *et al.*, 2010a; Środoń *et al.*, 2013). These findings justify regarding natural aluminoceladonite as an end-member in a continuous compositional series (Mg,Fe)-poor illite–Mg-rich illite–aluminoceladonite. This compositional series is observed mainly among finely dispersed, mostly interlayer-deficient, Al-rich K-dioctahedral 1*M* and 1*Md* mica varieties that occur in sedimentary rocks (Środoń and Eberl, 1984; Drits *et al.*, 2006, 2010a).

Although aluminoceladonite is often referred to as a rare mineral, its actual abundance may be underestimated because it is a mineral that can be overlooked easily. Based on XRD data, a *tv* 1*M* or 1*Md* mica with a $d_{001}$ parameter of 9.8–10.0 Å is readily identified as illite. Moreover, similar to illite, samples of aluminoceladonitic composition may have a small or moderate amount of smectite interlayers (Sokolova *et al.*, 1976; Drits and Kossovskaya, 1991; Drits and McCarty, 2007; Środoń *et al.*, 2013), which makes identification problematic.

The objectives of the present work were (1) to reveal diagnostic structural and crystal-chemical features that would allow distinction between (Mg,Fe)-poor illite, Mg-rich illite, and aluminoceladonite, and (2) to define the compositional ranges and identification criteria for the mica varieties in the series. For this purpose, the relationships between unit-cell parameters and cation composition were analyzed, and FTIR spectroscopy data were considered for illite and aluminoceladonite samples with a range of compositions from different environments.

## MATERIALS AND METHODS

### *Samples*

The samples studied range in composition from (Mg,Fe)-free illite to aluminoceladonite through Mg-rich illite (see Table 1 for the mineral identity, location, references to publications which list the mineralogical characteristics and the contents of expandable interlayers). The chemical compositions and the corresponding crystal-chemical formulae (Table 2) for samples RM30, M422, 10564, Zempleni, KJMC3, 60/3, 602-1, and 136 were taken from Drits *et al.* (2010a) and for the other samples, except aluminoceladonites Mal-4 and Mal-6, from the respective publications (Table 1).

Monomineral, <0.2 μm, Ca-exchanged, and dialyzed fractions of samples Mal-4 and Mal-6 were analyzed by inductively coupled plasma mass spectrometry (ICP-MS) as ignited samples fused with a Li metaborate-tetraborate flux at Activation Laboratories Ltd., Ancaster, Ontario, Canada. NIST 70a (K feldspar) and 76a (burnt refractory) standards were used to control accuracy (Table 3).

Samples 10564, 602-1, Z2, and 136 are smectite-free; the others contain small amounts of smectite interlayers (1–16%, Table 1). For samples RM30, M422, 10564, Zempleni, KJMC3, and 60/3, the expandable layer contents were determined by Drits *et al.* (2010a), and for other samples, they were taken from the respective publications (Table 1). For samples containing ⩾5% expandable layers, the corresponding molar contribution of the smectite layers to the average structural formula was subtracted according to the procedure described by Drits *et al.* (2010a) to provide the structural formulae for the mica-like components (Table 2).

Nineteen of the 22 samples have *trans*-vacant (*tv*) 1*M* or 1*Md* structures, sample 10564 has a *cis*-vacant (*cv*) 1*M* structure (Drits *et al.*, 2010a), sample SG4 is a *tv* $2M_1$ polytype (Eberl *et al.*, 1987), and sample IWi-1 is a mixture of $2M_1$, 1*Md*, and 1*M* polytypes (Grathoff *et al.*, 1995).

https://doi.org/10.1346/CCMN.2015.0630504 Published online by Cambridge University Press

Table 1. Sample description.

| # | Sample name | Mineral variety | Expandable layer content (%) | Origin; location; and reference |
|---|---|---|---|---|
| 1 | RM30 | illite (Mg, Fe)-poor | 5 | Miocene hydrothermal; Silverton Caldera, San Juan Mountains, Colorado; Eberl *et al.* (1987) |
| 2 | M422 | illite (Mg, Fe)-poor | 10 | Hydrothermally altered volcanics near gold deposit; Belgorod, Low Amur, Russia; Slonimskaya *et al.* (1978) |
| 3 | 10564 | illite (Mg, Fe)-poor | 0 | Hydrothermally altered sandstones around a uranium deposit, Athabasca basement; Saskatchewan, Canada; Drits *et al.* (1993) |
| 4 | SG4 | illite (Mg, Fe)-poor | 4 | Miocene hydrothermally altered volcanics, Silverton Caldera, San Juan Mountains, Colorado; Eberl *et al.* (1987) |
| 5 | RM35C | illite (Mg, Fe)-poor | 10.5 | Miocene hydrothermally altered volcanics, Silverton Caldera, San Juan Mountains, Colorado; Eberl *et al.* (1987) |
| 6 | Fuzz-5 | illite-smectite | 16 | Miocene hydrothermally altered volcanics; Fuzzeradvany, Hungary; Viczián (1997), Środoń *et al.* (2009b) |
| 7 | Fuzz-6 | illite-smectite | 16 | Miocene hydrothermally altered volcanics; Fuzzeradvany, Hungary; Viczián (1997), Środoń *et al.* (2009b) |
| 8 | Zempleni | illite-smectite | 15 | Miocene hydrothermally altered volcanics; Fuzzeradvany, Hungary; Viczián (1997), Środoń *et al.* (1992) |
| 9 | L-2A-1 | hairy illite Mg-rich | 1 | Triassic sandstone; Poland; Środoń and Eberl (1984) |
| 10 | Silver Hill | illite Mg-rich | 5 | Cambrian; CMS IMt-1; Środoń and Eberl (1984) |
| 11 | Swe-151 | illite-smectite | 13 | Ordovician K-bentonite; Röstånga, Sweden; Środoń *et al.* (2009a) |
| 12 | KJMC3 | illite Mg-rich | 5 | Ordovician K-bentonite; Vermont, USA; Ryan *et al.* (2007) |
| 13 | IWi-1 | illite | n.a. | Waukesha illite, Silurian; Wisconsin, USA; Grathoff *et al.* (1995) |
| 14 | 60/3 | globular illite Mg-rich | 5 | Clayey siltstones, Upper Riphean; South Urals, Russia; Ivanovskaya *et al.* (1989) |
| 15 | 60 | globular illite Mg-rich | 10 | Silty shales, Upper Riphean; South Urals, Russia; Ivanovskaya *et al.* (1989), Drits *et al.* (2013) |
| 16 | 602-1 | aluminoceladonite | 0 | Altered tuff in the Leeds Creek member of Twin Creek formation; Wyoming, USA; Drits *et al.* (2010a) |
| 17 | Z2 | aluminoceladonite | 0 | Devonian bentonite; Barcza, Poland; Seifert (1968), Kardymowicz (1960) |
| 18 | 99-3/5 | aluminoceladonite | 8 | Vitric tuff in saliferous strata; Inder, Russia; Sokolova *et al.* (1976) |
| 19 | 99-3/6 | aluminoceladonite | 8 | Vitric tuff in saliferous strata; Inder, Russia; Sokolova *et al.* (1976), Drits and McCarty (2007) |
| 20 | Mal-4 | aluminoceladonite | 9.5 | Silurian K-bentonite; Podolia, Ukraine; Środoń *et al.* (2013) |
| 21 | Mal-6 | aluminoceladonite | 8 | Silurian K-bentonite; Podolia, Ukraine; Środoń *et al.* (2013) |
| 22 | 136 | aluminoceladonite | 0 | Upper Jurassic conglomerates; Tushleg, Mongolia; Petrova and Amarjargal (1996) |

*XRD and determination of unit-cell parameters*

The XRD data and unit-cell parameters for samples RM30, M422, 10564, Zempleni, KJMC3, 60/3, 602-1, and 136 were obtained by Drits *et al.* (2010a), and for samples 99-3/6 and 60, by Drits and McCarty (2007) and Drits *et al.* (2013), respectively. For defect-free 1*M* structures, the unit-cell parameters were refined by the least-squares technique. For 1*Md* structures having a moderate amount of defects the parameters were evaluated by the trial-and-error method based on the equations relating $d_{001}$, $d_{060}$, $d_{11\bar{2}}$, $d_{112}$, $d_{22\bar{1}}$, and $d_{\bar{1}31}$ to *a*, *b*, *c*, and β (Sakharov *et al.*, 1990; Drits *et al.*, 2010a). Random powder XRD patterns for samples Mal-4 and Mal-6 were collected using a Bruker D8 diffractometer (Bruker AXS, Karlsruhe, Germany) (40 kV, 40 mA, Bragg-Brentano θ-θ mode with a 250 mm goniometer radius). Scans were made from 16.0 to 64.0°2θ , with a 0.05° step increment, and a count time of 180 s per step using $CuK\alpha_{1,2}$ radiation with a Ni filter; divergence, antiscatter, and detector slits were 0.5°, 0.5°, and 0.1°.

https://doi.org/10.1346/CCMN.2015.0630504 Published online by Cambridge University Press

Table 2. Cation compositions per $O_{10}(OH)_2$ of the samples studied.

| | | Cation composition | | | | | | | | | |
|---|---|---|---|---|---|---|---|---|---|---|---|
| | | Tetrahedral | | Octahedral | | | | Interlayer | | | |
| # | Sample | Si | Al | Al | $Fe^{3+}$ | $Fe^{2+}$ | Mg | K | Ca, Sr | Na | $NH_4$ |
| 1 | RM30 | 3.27 | 0.73 | 1.86 | 0 | 0 | 0.14 | 0.80 | 0.03 | 0.01 | n.a. |
| | mica component | 3.24 | 0.76 | 1.88 | 0 | 0 | 0.13 | 0.84 | 0.02 | 0.01 | |
| 2 | M422 | 3.22 | 0.78 | 1.92 | 0.01 | 0 | 0.09 | 0.74 | 0.03 | 0 | n.a. |
| | mica component | 3.15 | 0.85 | 1.96 | 0.01 | 0 | 0.05 | 0.83 | 0 | 0 | |
| 3 | 10564 | 3.27 | 0.73 | 1.86 | 0.04 | n.a. | 0.15 | 0.71 | 0.01 | 0.01 | n.a. |
| 4 | SG4 | 3.24 | 0.76 | 1.88 | 0.02 | n.a. | 0.10 | 0.79 | 0.01 | 0.05 | n.a. |
| 5 | RM35C | 3.30 | 0.70 | 1.82 | 0.05 | n.a. | 0.13 | 0.73 | 0.04 | 0.02 | n.a. |
| | mica component | 3.24 | 0.76 | 1.86 | 0.05 | | 0.09 | 0.82 | 0.01 | 0.02 | |
| 6 | Fuzz-5 | 3.38 | 0.62 | 1.83 | 0.01 | n.a. | 0.14 | 0.68 | 0.06 | 0 | 0.01 |
| | mica component | 3.29 | 0.71 | 1.88 | 0.01 | | 0.08 | 0.81 | 0.02 | 0 | 0.01 |
| 7 | Fuzz-6 | 3.42 | 0.58 | 1.75 | 0.02 | n.a. | 0.23 | 0.70 | 0.05 | 0 | 0.01 |
| | mica component | 3.34 | 0.66 | 1.81 | 0.02 | | 0.19 | 0.83 | 0 | 0 | 0.01 |
| 8 | Zempleni | 3.43 | 0.57 | 1.78 | 0.01 | n.a. | 0.22 | 0.66 | 0.03 | 0.03 | n.a. |
| | mica component | 3.36 | 0.64 | 1.82 | 0.01 | | 0.18 | 0.78 | 0 | 0 | |
| 9 | L-2A-1 | 3.45 | 0.55 | 1.57 | 0.13 | n.a. | 0.28 | 0.78 | 0.02 | 0.06 | n.a. |
| 10 | Silver Hill | 3.48 | 0.52 | 1.46 | 0.25 | 0.08 | 0.22 | 0.72 | 0 | 0.05 | n.a. |
| | mica component | 3.46 | 0.54 | 1.47 | 0.25 | 0.08 | 0.21 | 0.76 | 0 | 0.02 | |
| 11 | Swe-151 | 3.49 | 0.51 | 1.68 | 0.04 | n.a. | 0.27 | 0.58 | 0.06 | 0.01 | 0.06 |
| | mica component | 3.44 | 0.56 | 1.71 | 0.04 | | 0.24 | 0.67 | 0.02 | 0.01 | 0.07 |
| 12 | KJMC3 | 3.53 | 0.47 | 1.54 | 0.07 | 0.11 | 0.32 | 0.69 | 0.01 | 0.06 | n.a. |
| | mica component | 3.51 | 0.49 | 1.54 | 0.07 | 0.11 | 0.32 | 0.73 | 0.01 | 0.04 | |
| 13 | IWi-1 | 3.56 | 0.44 | 1.44 | 0.14 | n.a. | 0.39 | 0.72 | 0 | 0.16 | n.a. |
| 14 | 60/3 | 3.65 | 0.35 | 1.36 | 0.13 | 0.15 | 0.40 | 0.75 | 0.02 | 0.01 | n.a. |
| | mica component | 3.63 | 0.37 | 1.36 | 0.13 | 0.15 | 0.40 | 0.79 | 0 | 0.01 | |
| 15 | 60 | 3.63 | 0.37 | 1.32 | 0.13 | 0.16 | 0.46 | 0.77 | 0 | 0.01 | n.a. |
| | mica component | 3.59 | 0.41 | 1.33 | 0.13 | 0.16 | 0.43 | 0.85 | 0 | | |
| 16 | 602-1 | 3.71 | 0.29 | 1.39 | 0.04 | 0.09 | 0.51 | 0.75 | 0.01 | 0.03 | n.a. |
| 17 | Z2 | 3.81 | 0.19 | 1.19 | 0.06 | 0.17 | 0.57 | 0.86 | 0.04 | 0 | n.a. |
| 18 | 99-3/5 | 3.78 | 0.22 | 1.28 | 0.11 | 0.06 | 0.59 | 0.65 | 0.05 | 0.01 | n.a. |
| | mica component | 3.76 | 0.24 | 1.28 | 0.11 | 0.06 | 0.59 | 0.71 | 0.03 | 0.01 | |
| 19 | 99-3/6 | 3.80 | 0.20 | 1.18 | 0.25 | n.a. | 0.59 | 0.65 | 0.03 | 0.01 | n.a. |
| | mica component | 3.78 | 0.22 | 1.18 | 0.25 | n.a. | 0.59 | 0.71 | 0.01 | 0.01 | |
| 20 | Mal-4 | 3.84 | 0.16 | 1.33 | 0.09 | n.a. | 0.55 | 0.65 | 0.05 | 0.01 | 0.05 |
| | mica component | 3.82 | 0.18 | 1.33 | 0.09 | n.a. | 0.54 | 0.72 | 0.02 | 0.01 | 0.05 |
| 21 | Mal-6 | 3.86 | 0.14 | 1.29 | 0.09 | n.a. | 0.60 | 0.67 | 0.04 | 0.01 | 0.05 |
| | mica component | 3.82 | 0.15 | 1.29 | 0.09 | n.a. | 0.60 | 0.73 | 0.02 | 0.01 | 0.05 |
| 22 | 136 | 4.00 | 0 | 1.08 | 0.13 | 0.19 | 0.60 | 0.78 | 0 | 0.01 | n.a. |

Note. Unit-cell parameters determined for samples 1–3, 8, 10, 12, 14–16, and 19–22; FTIR spectra obtained for samples 1, 5–9, 11, 13, 15–18, and 20–22. The $TiO_2$ contents were excluded from the calculation of the crystal-chemical formulae. Cation compositions for the mica component are given for samples having >5% expandable layers.

Analysis of the experimental powder XRD patterns shows that the samples are monomineralic dioctahedral 1*M* mica varieties. The determination and refinement of the unit-cell parameters of the mica structures were carried out using experimental $d_{hkl}$ values. The unit-cell parameters were refined by the least-squares technique using the *Jade*® computer program (MDI, Inc.) (Table 4). To minimize the possible influence of expandable layers the experimental $d_{00l}$ values were excluded from the refinement procedure.

Table 3. Chemical composition of samples Mal-4 and Mal-6 (wt.%).

| Sample | N | C | H | $SiO_2$ | $Al_2O_3$ | $Fe_2O_3$ | MnO | MgO | CaO | $Na_2O$ | $K_2O$ | $TiO_2$ | LOI | Total |
|---|---|---|---|---|---|---|---|---|---|---|---|---|---|---|
| Mal-4 | 0.08 | 0.58 | 0.82 | 55.70 | 18.30 | 1.76 | 0.002 | 5.33 | 0.62 | 0.07 | 7.37 | 0.077 | 9.93 | 99.18 |
| Mal-6 | 0.09 | 0.46 | 0.77 | 56.26 | 17.69 | 1.78 | 0.003 | 5.89 | 0.56 | 0.05 | 7.72 | 0.099 | 9.6 | 99.65 |

https://doi.org/10.1346/CCMN.2015.0630504 Published online by Cambridge University Press

*FTIR spectroscopy*

The absorption spectra of samples RM30, RM35C, SG4, Zempleni, L-2A-1, 60, 602-1, Seifert, 99-3/5, and 136 were recorded with a Nicolet ESP-260 FTIR spectrometer (Thermo Fisher Scientific, Waltham, Massachusetts, USA) in the mid-IR (MIR) region (400−4000 $cm^{-1}$), using the sample-preparation technique, experimental procedure, and spectra manipulations described by Zviagina *et al.* (2004).

For samples Fuzz-5, Fuzz-6, Mal-4, and Mal-6, the IR spectra were obtained using a Bruker VERTEX 80v FTIR spectrometer (Bruker Optics, Ettlingen, Germany) equipped with a deuterated triglycine sulfate KBr detector and KBr beam splitter. For each sample, 256 scans were recorded under vacuum in the MIR region (400−4000 $cm^{-1}$) with a resolution of 4 $cm^{-1}$. To obtain a KBr pellet, 0.5 mg of sample was dispersed in 200 mg of KBr; the resulting mixture was placed in a 13 mm pellet die and pressed under vacuum for 10−15 min. The pellet was placed in a glass desiccant box with $CaCl_2$ and heated in a furnace at 105ºC for at least 20 h.

Spectra manipulations were performed using the *OPUS* 7.0 software package (Bruker Ltd.). Baseline correction was made automatically using the concave rubber band method with 64 baseline points and 10 iterations. The OH-stretching regions of selected spectra were decomposed and fitted according to the procedure reported by Zviagina *et al.* (2004).

## RESULTS

*Crystal-chemical data*

According to the crystal-chemical formulae, the mica structures form a continuous series, which can be divided, for the purpose of this analysis, into three groups. The first group, (Mg,Fe)-poor illites (mica components in #1−8, Table 2), includes samples in which octahedral cations are mostly Al (1.81−1.96 cations p.h.f.u.), with a minor amount of Mg (0.05−0.19 cations p.h.f.u.) (Table 2). The Fe cation contents are ⩽0.05 p.h.f.u.. The interlayer K deficiency, which is typical for illite, is mostly compensated by lower Al-for-Si substitution (0.64−0.85 cations p.h.f.u.) compared to ideal muscovite. The second group, Mg-rich illites (#9−15, Table 2), includes samples with phengite-like compositions having relatively high Mg content (0.21−0.43 cations p.h.f.u.) and relatively low Al-for-Si substitution (0.37−0.56 cations p.h.f.u., Table 2). In addition to Mg, these samples contain octahedral $Fe^{2+}$ (up to 0.16 cations p.h.f.u.) and/or $Fe^{3+}$ (0.04−0.25) (Table 2).

The samples of the third group (#16−22, Table 2) have compositions approaching aluminoceladonite with little or no tetrahedral Al (0−0.29 cations p.h.f.u., Table 2) and large amounts of octahedral Mg (0.51−0.60 cations p.h.f.u., Table 2). In addition, these samples contain octahedral $Fe^{2+}$ (0.06−0.19 cations

Table 4. Unit-cell parameters of (Mg, Fe)-poor illites, Mg-rich illites, and aluminoceladonites (sample numbers as in Tables 1 and 2).

| | (Mg,Fe)-poor illites | | | | | Mg-rich illites | | | Aluminoceladonites | | | | |
|---|---|---|---|---|---|---|---|---|---|---|---|---|---|
| # | 1 | 2 | 3 | 8 | 10 | 12 | 14 | 15 | 16 | 19 | 20 | 21 | 22 |
| Sample | RM30 | M422 | 10564 | Zempleni | Silver Hill | KJMC3 | 60/3 | 60 | 602-1 | 99-3/6 | Mal-4 | Mal-6 | 136 |
| $a$ (Å) | 5.2021 | 5.1994 | 5.1973 | 5.2042 | 5.208 | 5.210 | 5.235 | 5.220 | 5.2141 | 5.226 | 5.227 | 5.215 | 5.2227 |
| $b$ (Å) | 8.9797 | 8.9815 | 8.999 | 8.9852 | 9.020 | 9.020 | 9.032 | 9.042 | 9.0082 | 9.000 | 9.011 | 9.013 | 9.0195 |
| $c$ (Å) | 10.226 | 10.233 | 10.147 | 10.205 | 10.166 | 10.159 | 10.14 | 10.156 | 10.108 | 10.090 | 10.102 | 10.093 | 10.076 |
| β (º) | 101.57 | 101.60 | 99.00 | 101.49 | 101.5 | 101.4 | 101.52 | 101.27 | 101.12 | 100.8 | 101.2 | 101.1 | 100.82 |
| $c\sin\beta$(Å) | 10.018 | 10.024 | 10.022 | 10.000 | 9.962 | 9.959 | 9.936 | 9.960 | 9.918 | 9.911 | 9.910 | 9.905 | 9.897 |
| $c\cos\beta/a$ | −0.394 | −0.396 | −0.305 | −0.391 | −0.389 | −0.385 | −0.387 | −0.380 | −0.374 | −0.362 | −0.362 | −0.372 | −0.362 |

https://doi.org/10.1346/CCMN.2015.0630504 Published online by Cambridge University Press

p.h.f.u.) and/or $Fe^{3+}$ (0.04–0.25 cations p.h.f.u.), and the total amount of divalent octahedral cations (Mg + $Fe^{2+}$) varies from 0.54 to 0.79 cations p.h.f.u. (Table 2). The cation composition of sample 602-1 is intermediate between those of samples 60 and 99-3/5 (Table 2); the reasons for including it in the aluminoceladonite group will be discussed below. The total layer charge of the mica components in the three groups is similar and varies slightly around 0.8.

*XRD data*

Except for sample 10564, which is *cv* (Mg,Fe)-poor illite with the strongest peak 110 and four reflections of similar intensity, 111, 11$\bar{2}$, 112, and 11$\bar{3}$, in the 02*l*, 11*l* region, the powder XRD patterns from the samples of all the three groups (Figure 1) show reflection positions and intensity distributions typical of *tv* 1*M* micas: the 02*l*, 11*l* region contains the most intense 020 peak and strong reflections 11$\bar{1}$, 11$\bar{2}$, and 112, with a much weaker 11$\bar{3}$ peak (Zviagina *et al.*, 2007). Closer inspection, however, reveals differences in reflection positions, the most important being significantly lower $d_{003}$ and $d_{005}$ values in aluminoceladonites (*e.g.* 3.299 Å and 1.979 Å, respectively, in sample 136), as compared with those for (Mg,Fe)-poor illite (*e.g.*, 3.339 Å and 2.003 Å, respectively, sample RM30), whereas Mg-rich illites

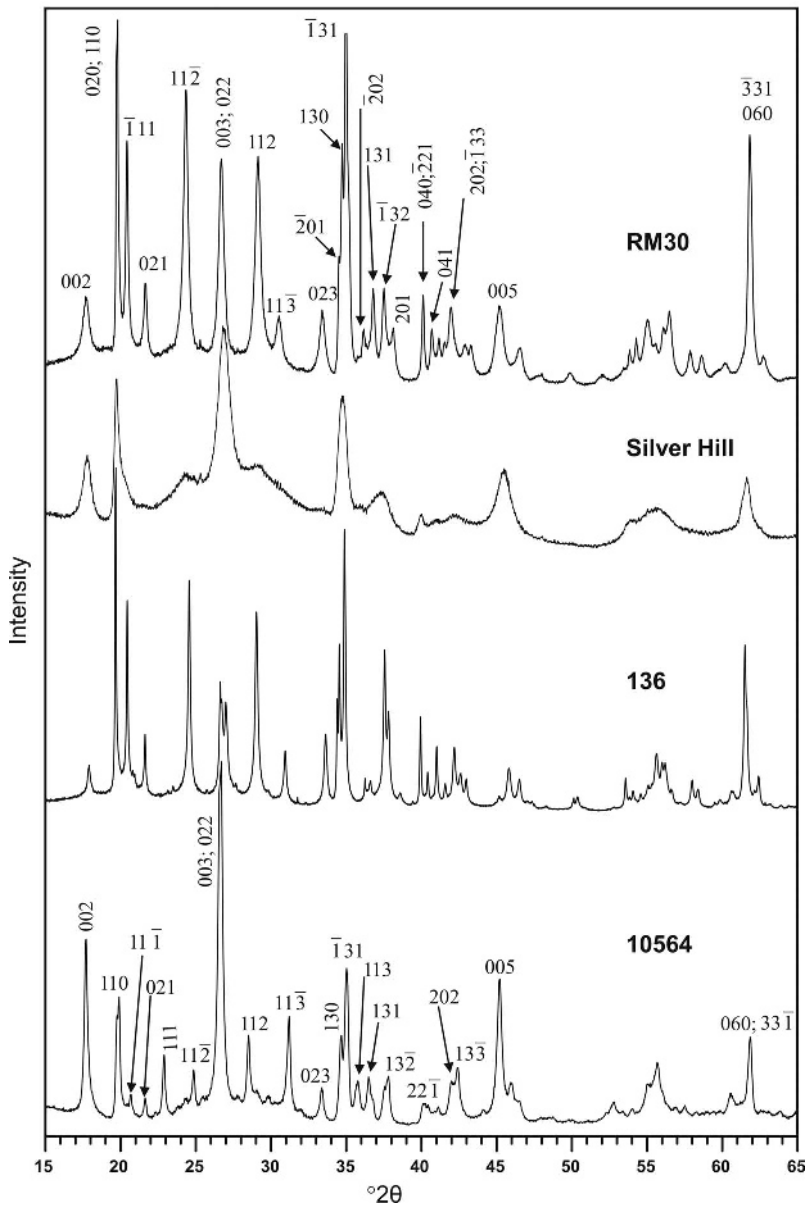


Figure 1. Powder XRD patterns for (Mg, Fe)-poor illite RM30, Mg-rich illite Silver Hill, aluminoceladonite 136, and *cv* illite 10564 (modified from Drits *et al.*, 2010a).

https://doi.org/10.1346/CCMN.2015.0630504 Published online by Cambridge University Press

have intermediate values (*e.g.* 3.325 Å and 1.993 Å, sample Silver Hill). The 003 and 022 reflections are therefore both resolved in the aluminoceladonite XRD patterns and they overlap in the illite samples (Figure 1). These differences in the positions of 003 and 005 reflections are also evident in the XRD patterns from oriented specimens if the number of expandable layers is <5%. More reliable conclusions, however, should be made based on the random powder XRD data.

*Unit-cell parameters.* The (Mg,Fe)-poor illite structures are characterized by relatively large layer-to-layer distances ($c\sin\beta$ = 10.018–10.024 Å) and relatively small lateral dimensions ($a$ = 5.197–5.204 Å, $b$ = 8.980–8.999 Å); the layer displacement values, $c\cos\beta/a$, are −0.391 to −0.396 for *tv* samples RM30, M422, and Zempleni, and −0.305 for the *cv* sample 10564 (Table 4). The Mg-rich illite structures have lower $c\sin\beta$ values (9.936–9.962 Å), larger lateral dimensions ($a$ = 5.208–5.235 Å, $b$ = 9.020–9.042 Å) and $c\cos\beta/a$ values of −0.389 to −0.380. Aluminoceladonite samples show reduced layer-to-layer distances ($c\sin\beta$ = 9.897–9.918 Å) and layer displacements ($|c\cos\beta/a|$ = 0.362–0.374). The lateral dimensions of the aluminoceladonites ($a$ = 5.214–5.232 Å, $b$ = 9.000–9.020 Å) are lower than those of the Mg-rich illites and similar to or slightly greater than those of the (Mg,Fe)-poor illites.

### *FTIR spectroscopy*

The positions of the absorption bands in the FTIR spectra of the samples in the MIR region were assigned to specific vibration modes (Table 5) following the interpretations of Farmer (1974), Velde (1978, 1980), Russell and Fraser (1994), Besson and Drits (1997a, 1997b), Madejová and Komadel (2001), and Madejová (2003). The FTIR spectra of all the samples are typical of dioctahedral micas. The region 600–950 $cm^{-1}$ shows the AlOHAl bending mode at 910–915 $cm^{-1}$, AlOHMg bending mode at 835–840 $cm^{-1}$ coupled with Al–O out-of-plane vibration at 820–830 $cm^{-1}$, bands at 695–700 $cm^{-1}$ (Si–O), and Al–O–Si in-plane and coupled Al–O and Si–O out-of-plane vibrations (in samples with Al-for-Si substitution) at 750–755 $cm^{-1}$ and ~620 $cm^{-1}$, respectively. The distinguishing features for the three groups of mica varieties are largely the most intense absorption band due to the Si–O stretching mode at ~1000 $cm^{-1}$, and three characteristic sharp bands in the Si–O bending region (400–550 $cm^{-1}$), as well the band positions and profile in the OH-stretching region with the maximum intensity at ~3600–3630 $cm^{-1}$ (Figure 2, Table 5).

*(Mg,Fe)-poor illites.* In most cases, the Si–O stretching mode is a strong asymmetric band at 1023–1027 $cm^{-1}$ with a shoulder at 1066–1082 $cm^{-1}$ corresponding to the Si–O apical stretching vibration (Figure 2, Table 5). In sample Fuzz-5, the latter is observed as a resolved maximum at 1090 $cm^{-1}$ (Table 5). The three characteristic bands in the Si–O bending region are located at 414–425, 471–477, and 525–535 $cm^{-1}$. These bands are interpreted as Si–O, Si–O–Si, and Al–O–Si (Kloprogge *et al.*, 1999; Madejová and Komadel, 2001) bending vibrations. The OH–stretching region shows a relatively broad band, which is a superposition of individual cation-OH-cation vibrations (mostly AlOHAl and AlOHMg), with a maximum at 3620–3629 $cm^{-1}$ (Figures 2a, 3a).

Table 5. Selected characteristic bands in the MIR region of the FTIR spectra of illites and aluminoceladonites ($cm^{-1}$) (sample numbers as in Tables 1 and 2).

| # | Sample | Si–O bend | Si–O–Si bend | Si–O–Al bend | Al–O–Si in-plane | Si–O stretch | Si–Oap stretch | OH-stretch, maximum absorption |
|---|---|---|---|---|---|---|---|---|
| 1 | RM30 | 414 | 477 | 534 | 754 | 1023 | 1066sh | 3629 |
| 4 | SG4 | 414 | 477 | 535 | 754 | 1024 | 1067sh | 3627 |
| 5 | RM35C | 415 | 476 | 533 | 755 | 1023 | 1068sh | 3629 |
| 6 | Fuzz-5 | 418 | 474 | 534 | 754 | 1024 | 1090 | 3630 |
| 7 | Fuzz-6 | 425 | 471 | 525 | 753 | 1027 | 1082sh | 3625 |
| 8 | Zempleni | 423 | 474 | 529 | 754 | 1027 | 1070sh | 3624 |
| 9 | L-2A-1 | 419 | 472 | 523 | 751 | 1021 | 1075 | 3618 |
| 11 | Swe-151 | 422 | 472 | 524 | 752 | 1019 | 1088sh | 3626 |
| 13 | IWi-1 | 424 | 472 | 520 | 752 | 1015 | 1090 | 3617 |
| 15 | 60 | 431 | 469 | 517 | 750 | 1006 | 1086 | 3606 |
| 16 | 602-1 | 436 | 470 | 518 | 754* | 1007 | 1091 | 3601 |
| 17 | Z2 | 437 | 472 | 512 | 750 | 989 | 1090 | 3603 |
| 18 | 99-3/5 | 435 | 470 | 520 | – | 1012 | 1098 | 3605 |
| 20 | Mal-4 | 435 | 470 | 518 | 754* | 1010 | 1090 | 3606 |
| 21 | Mal-6 | 435 | 470 | 518 | 752* | 1006 | 1091 | 3603 |
| 22 | 136 | 439 | 468 | 509 | – | 985 | 1112 | 3602 |

* – weak, sh = shoulder

https://doi.org/10.1346/CCMN.2015.0630504 Published online by Cambridge University Press

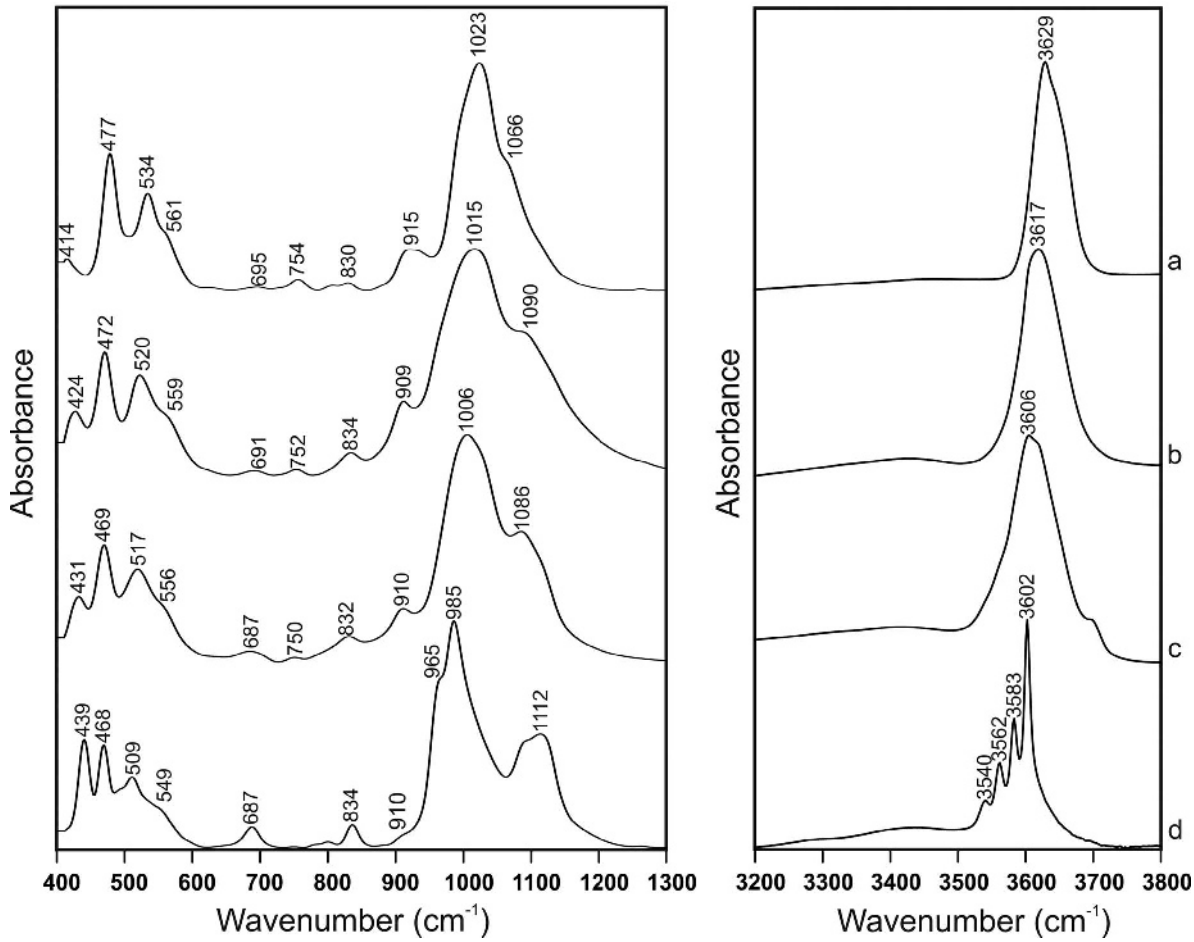


Figure 2. Selected FTIR spectra of illite and aluminoceladonite samples in the regions 400–1300 and 3200–3800 $cm^{-1}$ (a – RM30; b – IWi-1; c – 60, d – 136).

*Mg-rich illites.* The Si–O stretching vibration is located at 1006–1021 $cm^{-1}$, with the Si–O apical stretching mode either as a shoulder or as a resolved peak at 1075–1090 $cm^{-1}$ (Table 5, Figure 2b,c). The three bands in the Si–O bending region are at 419–431, 469–472, and 517–524 $cm^{-1}$. The maximum absorption in the OH-stretching region is at 3617–3626 $cm^{-1}$. Sample 60 is an exception, with the maximum intensity in the OH-stretching region at 3606 $cm^{-1}$ (Table 5, Figure 2b,c; Figure 3b).

*Aluminoceladonites.* The strongest Si–O stretching vibration is located at 985–1012 $cm^{-1}$, and the Si–O apical stretching mode is a resolved band at 1090–1112 $cm^{-1}$ (Table 5, Figure 2d). The Si–O bending region displays three bands at 435–439, 468–472, and 509–520 $cm^{-1}$. In samples 136 and Z2, the OH-stretching region consists of several sharp well resolved peaks, the most intense at 3602–3603 $cm^{-1}$ (AlOHMg), and MgOHMg, $AlOHFe^{2+}$, and $Fe^{3+}OHFe^{3+}$ at 3583, 3559–3562, and 3538–3540 $cm^{-1}$, rspectively. In addition, AlOHAl and $Fe^{2+}OHFe^{3+}$ bands are revealed by spectrum deconvolution and curve-fitting (Figure 3c). In the other aluminoceladonites, the OH-stretching region contains a wide absorption band resulting from superposition of individual cation-OH-cation vibrations with one sharp maximum at 3601–3606 $cm^{-1}$ (Table 5, Figure 3d). The individual bands are assigned to specific cation-OH-cation pairs according to the work of Besson and Drits (1997a, 1997b).

## DISCUSSION

### *Unit-cell parameters*

*Layer-to-layer distance.* The compositional variation from (Mg,Fe)-poor illite to aluminoceladonite through Mg-rich illite is accompanied by structural differences including a consistent decrease in the layer-to-layer distance. Typical $c\sin\beta$ values are near 10.02 Å for the (Mg,Fe)-poor group and 9.94 Å for Mg-rich illite, whereas for aluminoceladonite, $c\sin\beta$ is ~9.9 Å (Table 4). The dependence of $c\sin\beta$ on the amount of tetrahedral Al cations in the (Mg,Fe)-poor illite–aluminoceladonite series (Figure 4) is described by the equation:

https://doi.org/10.1346/CCMN.2015.0630504 Published online by Cambridge University Press

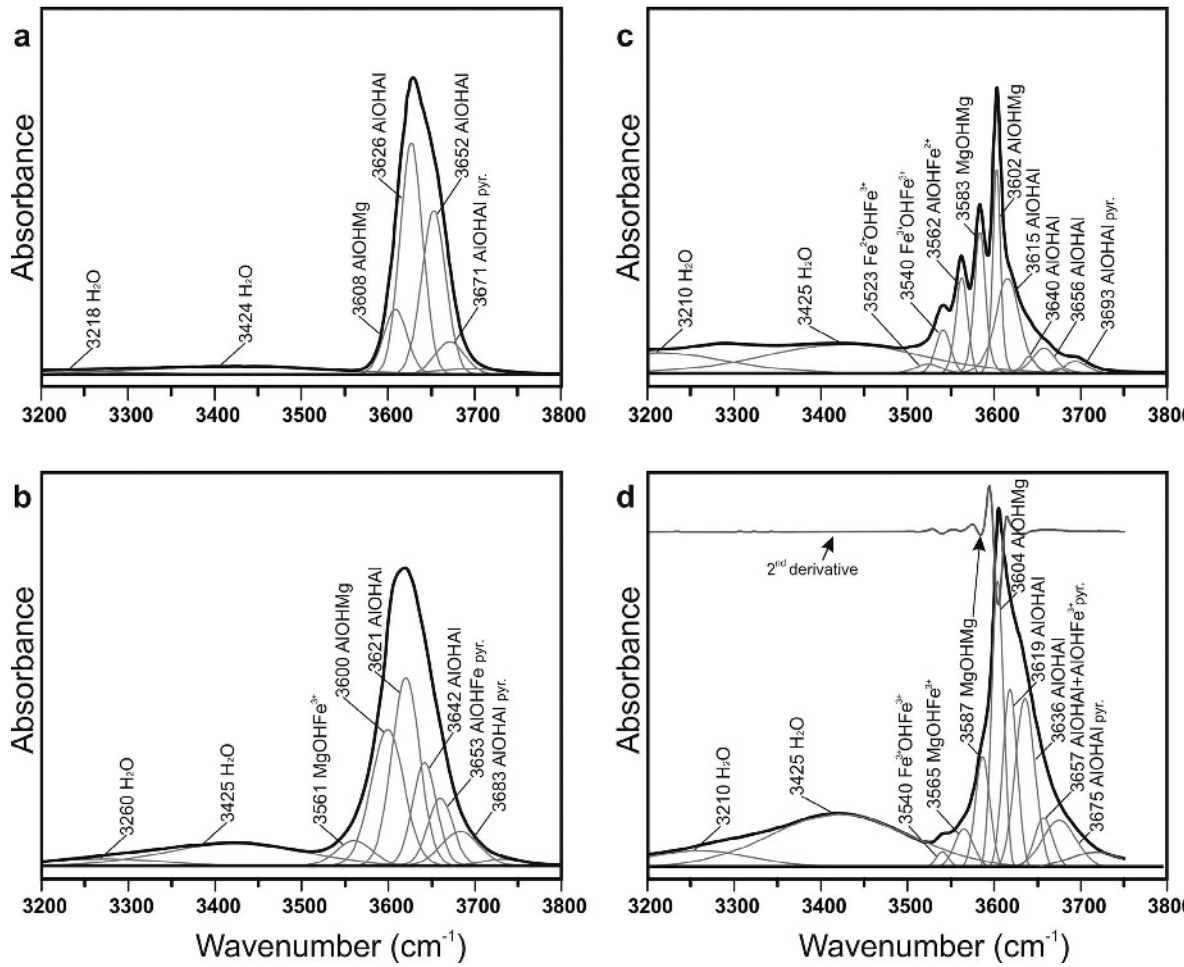


Figure 3. Decomposition and curve-fitting of the FTIR spectra of illite and aluminoceladonite samples in the OH-stretching region: a – RM30; b – IWi-1; c – 136; d – Mal-6. For sample Mal-6, the MgOHMg stretching mode is shown in the second derivative.

$$c\sin\beta = 9.896 + 0.172(^{IV}Al)^{1.5} \quad (1)$$

(estimated standard deviation, e.s.d. = 0.004 Å; the correlation coefficient, $R^2 = 0.991$), where $^{IV}Al$ is the tetrahedral Al content.

In order to provide insight into the factors controlling the contraction of the mica layer, Drits *et al.* (2010a) analyzed the structural features for a number of 1*M* and 1*Md* mica samples in the illite–aluminoceladonite series. With increasing Si and Mg contents, the mean octahedral sheet thickness was shown to increase whereas the mean tetrahedral sheet thickness decreases slightly within a very narrow interval. As a result, the mean thickness of the 2:1 layer increases slightly with decreasing *c*sinβ. Simultaneously, the mean interlayer distance decreases. The decrease in *c*sinβ does not, therefore, depend on the 2:1 layer thickness and is basically determined by the mean interlayer distance, which in turn depends on the amount of Al-for-Si substitution. Decreasing tetrahedral Al-for-Si substitution leads to a decrease in the under-saturation of the

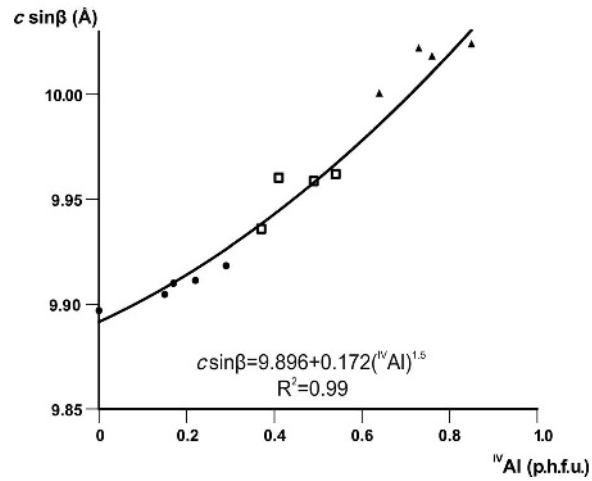


Figure 4. The *c*sinβ values in the series aluminoceladonite-illite plotted *vs.* tetrahedral Al contents. Symbols: triangle = (Mg,Fe)-poor illites, square = Mg-rich illites, circle = aluminoceladonites.

https://doi.org/10.1346/CCMN.2015.0630504 Published online by Cambridge University Press

basal oxygen atoms with respect to negative charge and, consequently, to weakening of their mutual repulsion. Accordingly, aluminoceladonites with little or no tetrahedral Al have shorter interlayer distances and as a result, reduced $c\sin\beta$ values.

*Layer displacement.* With increasing Mg contents in the series of *tv* illite-aluminoceladonite the absolute value of the layer displacement $|c\cos\beta/a|$ decreases from 0.396 (Mg = 0.05 cations p.h.f.u., sample M422) in (Mg,Fe)-poor illite to 0.362 (Mg = 0.60, sample 136) in aluminoceladonite (Table 4). The factors controlling the decrease in $|c\cos\beta/a|$ were analyzed by Drits *et al.* (2006). In a distorted dioctahedral mica structure, $|c\cos\beta/a| > a/3$ because the apical oxygens of the opposed tetrahedral sheets of the 2:1 layer are linked to elongated diagonal octahedral edges common to occupied and vacant octahedra (Figure 5a). As a result, the displacement of the center of the ditrigonal ring of the upper tetrahedral sheet with respect to that of the lower sheet, as measured across the vacant octahedral site, is $<2a/3$ (Figure 5b), and the intralayer displacement, which is the major component of the layer displacement, as measured across the pair of adjacent occupied octahedra, is $>a/3$. The greater the size difference between the occupied and the vacant octahedra, the greater the layer displacement. With increasing amounts of larger Mg cations, the size difference in question decreases, and so decreases the absolute value of the layer displacement. The dependence of $c\cos\beta/a$ on the amount of Mg cations p.h.f.u. (Figure 6) is described, with e.s.d. = 0.005 and $R^2 = 0.89$, by the regression equation:

$$c\cos\beta/a = 0.084Mg^2 + 0.002Mg - 0.396 \qquad (2)$$

where *Mg* is the octahedral Mg cations content (p.h.f.u.).

*The b parameter.* The dependence of *b* on the cation composition in the illite–aluminoceladonite series is not straightforward: *b* increases from (Mg,Fe)-poor illite to Mg-rich illite and then decreases from Mg-rich illite to aluminoceladonite. The actual lateral dimensions of the mica structure can be seen as a compromise between the larger dimensions of the idealized unrotated tetrahedral sheet and the smaller dimensions of the octahedral sheet, $b_t$ and $b_{oct}$, which are related to the tetrahedral basal and octahedral unshared lateral edge lengths, $(O-O)_{basal}$ and $(O-O)_{lateral}$, respectively by: $b_t = 2\sqrt{3}(O-O)_{basal}$; $b_{oct} = 3(O-O)_{lateral}$.

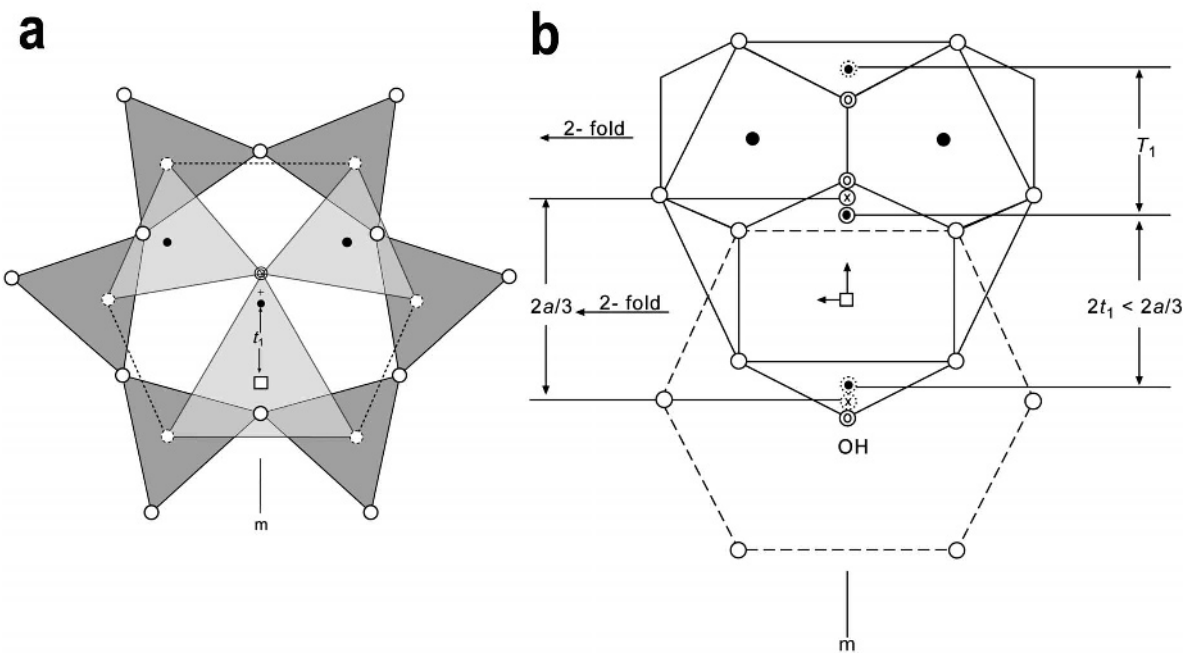


Figure 5. (a) Projection on the *ab* plane of a fragment of the upper part of the *tv* 2:1 layer (below) and cross-section of the tetrahedral sheet (above). Shared apical oxygen atoms are shown as dashed circles. Open circles represent basal oxygens; the double circle, an hydroxyl; the quadrangle, a vacant octahedral site; larger black circles, octahedral cations; the smaller black circle indicates the center of the ditrigonal tetrahedral ring; and the cross indicates the position of the center of a ring with $\alpha = 0$; $t_1$ is the distance between the centers of the tetrahedral ring and vacant *trans* octahedron, m is the symmetry plane; (b) projection on the *ab* plane of a fragment of the *tv* 2:1 layer showing that the center of the upper tetrahedral ditrigonal ring is shifted with respect to that of the lower sheet by $2t_1 < 2a/3$, as measured across the vacant octahedral site, and that the intralayer stagger, as measured across the pair of adjacent occupied octahedra, is $T_1 = |2t_1 - a| > a/3$. Open circles represent apical oxygens; large black circles, octahedral cations; double circles, hydroxyls; the quadrangle indicates the center of the vacant octahedron; black circles in dotted and open circles indicate centers of the lower and upper ditrigonal tetrahedral rings, respectively; crosses in dotted and open circles indicate centers of the lower and upper tetrahedral rings with $\alpha = 0$, respectively (after Drits *et al.*, 2006).

https://doi.org/10.1346/CCMN.2015.0630504 Published online by Cambridge University Press

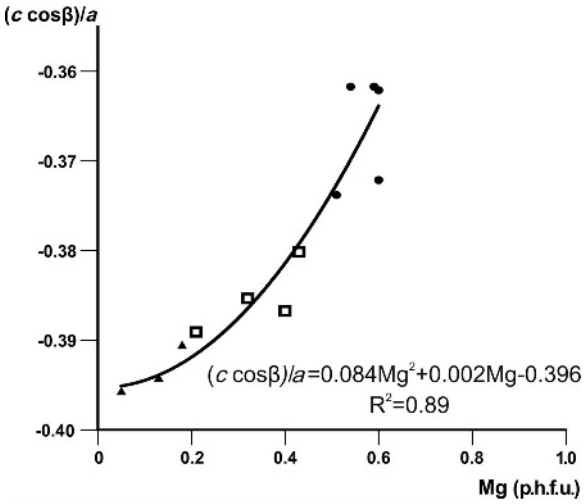


Figure 6. The *c*cosβ/*a* values in the series aluminoceladonite–illite plotted *vs.* octahedral Mg contents. Symbols as in Figure 4.

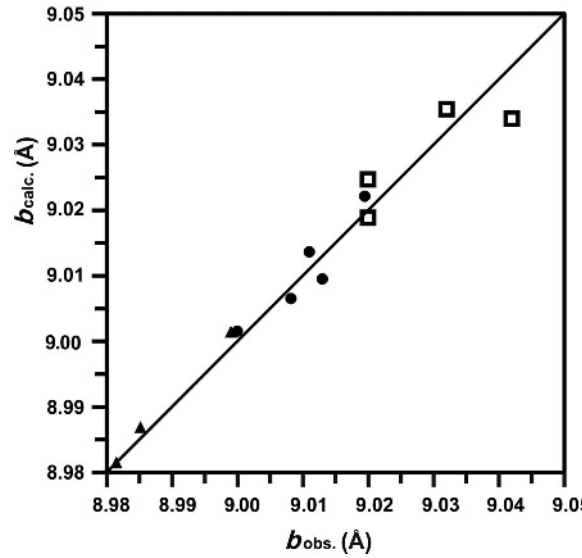


Figure 7. Calculated *b* parameters plotted *vs.* observed values. Symbols as in Figure 4.

With increasing Si contents, the tetrahedral size decreases while tetrahedral elongation increases (Drits *et al.*, 2010a; Zviagina and Drits, 2012), and, as a result, $(O-O)_{basal}$ decreases. Simultaneously, increasing contents of larger octahedral cations ($Mg,Fe^{2+},Fe^{3+}$) lead to increasing $(O-O)_{lateral}$ values. In the transition from (Mg,Fe)-poor illite to Mg-rich illite, the second of these trends dominates, and *b* increases; in the Mg-rich illite–aluminoceladonite series, the decrease in $(O-O)_{basal}$ begins to dominate, and *b* decreases. The observed relationship between *b* and octahedral cation composition in the illite–aluminoceladonite series is described, with e.s.d. = 0.005 Å; $R^2$ = 0.963 (Figure 7), by the equation

$$b = 9.039 - 0.121(Mg - 0.287)^2 - 0.689(Fe^{2+} - 0.116)^2 - 1.994(Fe^{3+} - 0.154)^2 \quad (3)$$

where *Mg*, $Fe^{2+}$, and $Fe^{3+}$ are the contents of the corresponding octahedral cations p.h.f.u.

The relatively large *b* value in aluminoceladonite 136 (9.0195 Å) is associated with a significant amount of large $Fe^{2+}$ cations.

Each of the three groups of micas in the illite–aluminoceladonite series is characterized, therefore, by a unique combination of unit-cell parameter variation ranges (Table 6). In particular, the distinctive features of aluminoceladonite are reduced values of *c*sinβ and |*c*cosβ/*a*| in combination with *b* parameters that are lower than those for Mg-rich illites and only slightly greater than those for (Mg,Fe)-poor illites. For this reason, sample 602-1, which is intermediate in composition between Mg-rich illite sample 60 and aluminoceladonite sample 99-3/5, should be classified as aluminoceladonite. The boundary from illite to aluminoceladonite occurs therefore around the Si contents of ~3.7 p.h.f.u. and ($Mg + Fe^{2+}$) contents of ~0.6 cations p.h.f.u.

### *FTIR spectroscopy data*

*Si–O vibrations.* According to Farmer (1974), the Si–O stretching vibrations are only weakly coupled with other vibrations of the structure, whereas the Si–O bending vibrations are strongly coupled with vibrations of the octahedral cations and with translator vibrations of hydroxyl groups. In both regions, however, strong correlations are observed between the spectroscopic characteristics and both tetrahedral and octahedral cation composition. Considering these correlations the cation

Table 6. The compositional ranges (cations p.h.f.u.) and identification criteria for (Mg,Fe)-poor illite, Mg-rich illite, and aluminoceladonite.

| | (Mg,Fe)-poor illite | Mg-rich illite | Aluminoceladonite |
|---|---|---|---|
| Si | <3.4 | 3.4–3.7 | >3.7 |
| $Mg+Fe^{2+}$ | <0.2 | 0.2–0.6 | ⩾0.6 |
| *c*sinβ, Å | 9.98–10.02 | 9.94–9.96 | 9.90–9.92 |
| \|*c*cosβ/*a*\| | ~0.40 (*tv*); ~0.30 (*cv*) | 0.38–0.39 (*tv*) | 0.36–0.37 (*tv*) |
| *b*, Å | 8.98–9.00 | 9.02–9.04 | 9.00–9.02 |

https://doi.org/10.1346/CCMN.2015.0630504 Published online by Cambridge University Press

compositions from the bulk crystal-chemical formulae (Table 2) are used because the IR vibration modes are sensitive to the cation distribution in both mica and smectite layers. With decreasing Al-for-Si substitution in the (Mg,Fe)-poor illite–Mg-rich illite–aluminoceladonite series, the Si–O stretching band, $\nu_{SiO}$, shifts from 1024 $cm^{-1}$ ($^{IV}Al$ = 0.76, sample SG-4) to 985 $cm^{-1}$ ($^{IV}Al$ = 0, sample 136), and the Si–O apical stretching mode, $\nu_{SiOap}$, transforms from a shoulder at 1067 $cm^{-1}$ into a well-resolved band at 1112 $cm^{-1}$ (Table 5, Figure 2). With increasing Si and decreasing octahedral Al contents, the non-bridging tetrahedral cation–anion ($T-O_{apical}$) distance is significantly shortened and the bond strengthened with respect to the mean bridging ($T-O_{basal}$) distance due to increasing under-saturation of the apical oxygen anion with respect to negative charge. This effect is confirmed by numerous structure refinements of dioctahedral micas-2$M_1$ (*e.g.* Rothbauer, 1971; Ivaldi *et al.*, 2001; Smyth *et al.*, 2000) and can be described quantitatively in terms of the bond-strength sum variation (Zviagina and Drits, 2012). Accordingly, the two Si–O stretching modes become resolved, as $\nu_{SiO}$ shifts to lower and $\nu_{SiOap}$ to greater wavenumbers. Both trends can be described by quadratic regressions relating $\nu_{SiO}$ and $\nu_{SiOap}$ to $^{IV}Al$ (Figure 8a,b), with the correlation coefficients $R^2$ = 0.76 and 0.77, respectively. A much stronger correlation is observed between $\nu_{SiO}$ and octahedral Al contents, $^{VI}Al$ ($R^2$ = 0.94, Figure 9). The positions and profile of Si–O stretching vibrations, however, can only serve as identification criteria if the spectra are recorded in transmission mode from KBr pellets with low-density dilution, because of the possible influence of various instrumental factors (Derkowski, 2015, pers. comm.).

Simultaneously, with increasing Si contents from (Mg,Fe)-poor illite to aluminoceladonite, the two 'outer' bands in the Si–O bending vibrations triplet move toward the 'middle' one, so that the lower- and the higher-wavenumber bands (denoted here as $\delta_1$ and $\delta_3$, respectively) are shifted from 414 to 439 $cm^{-1}$ and from 535 to 509 $cm^{-1}$, respectively; the wavenumber of the 'middle' Si–O–Si bending vibration, $\delta_2$, decreases slightly from 477 to 468 $cm^{-1}$ (Figures 3, 10; Table 5). The regularities observed in the regions of Si–O stretching and bending vibrations are similar to those in the spectra presented by Velde (1978) for the transition from synthetic muscovite to synthetic aluminoceladonite, although Velde (1978) only discussed the shifts of $\nu_{SiOap}$ and $\delta_3$ to greater and lower wavenumbers, respectively.

A possible explanation for the band shifts in the Si–O bending region in the (Mg,Fe)-poor illite–Mg-rich illite–aluminoceladonite series is provided by a comparison of the spectra of samples RM30 and 136 (Mg,Fe-poor illite and aluminoceladonite, respectively)

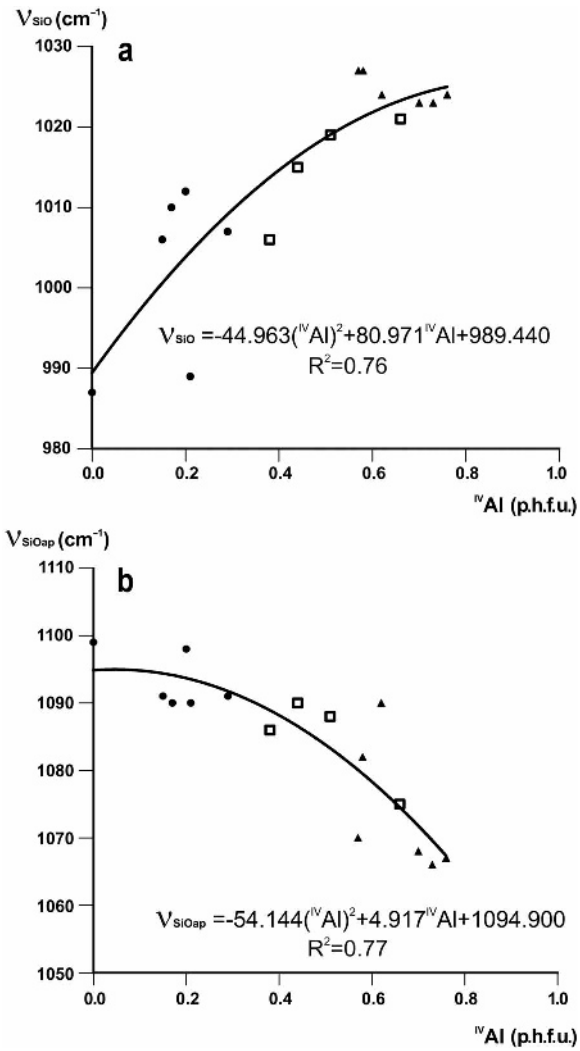


Figure 8. Band positions ($cm^{-1}$) of (a) $\nu_{SiO}$ and (b) $\nu_{SiOap}$ plotted *vs.* $^{IV}Al$ contents (cations p.h.f.u.). Symbols as in Figure 4.

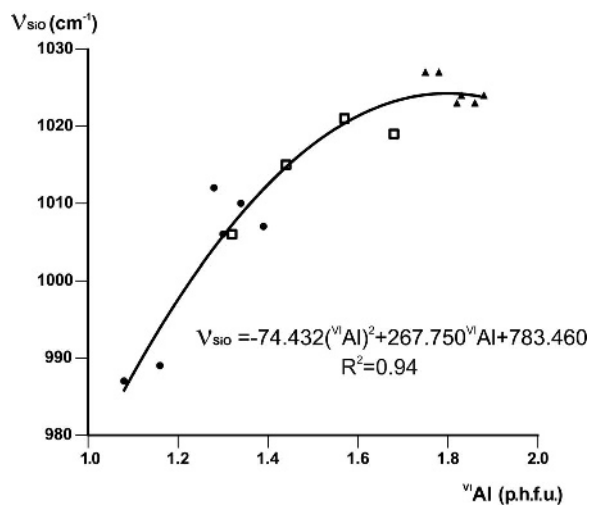


Figure 9. Band positions ($cm^{-1}$) of $\nu_{SiO}$ plotted *vs.* $^{VI}Al$ contents (cations p.h.f.u.). Symbols as in Figure 4.

https://doi.org/10.1346/CCMN.2015.0630504 Published online by Cambridge University Press

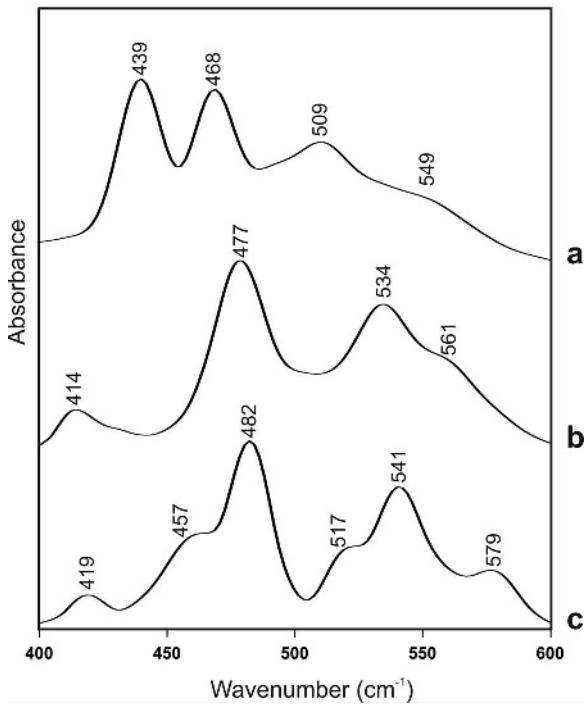


Figure 10. FTIR spectra of (a) aluminoceladonite 136, (b) illite RM30, and (c) pyrophyllite (North Carolina) in the Si-O bending region (400–600 $cm^{-1}$).

with that of pyrophyllite $Al_2Si_4O_{10}(OH)_2$ (Figure 10) in the region 400–550 $cm^{-1}$. Owing to the identical tetrahedral cation composition, the spectrum of aluminoceladonite in the region of Si–O bending vibrations might be expected to be similar to that of pyrophyllite. In reality, however, the band positions in spectra of aluminoceladonite 136 and pyrophyllite differ dramatically: 439 *vs*. 419, 468 *vs*. 482 and 509 *vs*. 541 $cm^{-1}$ (Figure 10a,c). At the same time, the maximum absorption in the pyrophyllite spectrum is observed at positions close to those of the illites of muscovite-like composition having 0.70–0.85 $^{IV}$Al (*e.g.* 414, 477, and 534 $cm^{-1}$, sample RM30) (Figure 10b). These results may imply that the influence of octahedral cation composition on the band positions in the Si–O bending region is stronger than that of the composition of the tetrahedral sheet and the presence or absence of the interlayer cations.

The shift of the Si–O bending mode, $\delta_1$, to greater wavenumbers in the illite–aluminoceladonite series may be associated with the growing influence of the Mg–O stretching vibration (Beran *et al.* (2004) assign the band at 437 $cm^{-1}$ in silicate structures to Mg–O stretch + O–Si–O bend), taking into account that the relative intensity of $\delta_1$ with respect to $\delta_2$ increases with increasing Mg contents (Figure 10). The correlations between the position of this band and $^{IV}$Al and Mg contents are equally strong and described by a quadratic and linear regression, respectively (Figure 11):

$$\delta_1 = -26.026(\,^{IV}Al\,)^2 - 15.001\,^{IV}Al + 439.25 \quad (R^2 = 0.95) \quad (4)$$

$$\delta_1 = 45.134Mg + 410.07 \quad (R^2 = 0.93) \quad (5)$$

Equations 4 and 5 can be used to evaluate the amount of $^{IV}$Al and Mg with an e.s.d. of 0.06 and 0.05 cations p.h.f.u., respectively (Table 7).

The absorption band $\delta_2$ is interpreted as the Si–O–Si bending vibration (Madejova and Komadel, 2001, Madejova, 2003) coupled with the Al–O–Al bend (Beran *et al.*, 2004). The wavenumber decrease of $\delta_2$ with decreasing tetrahedral and octahedral Al and increasing octahedral Mg contents is described by quadratic regression equations with $R^2$ = 0.77, 0.77 and 0.81, respectively with considerable scatter (Figure 12).

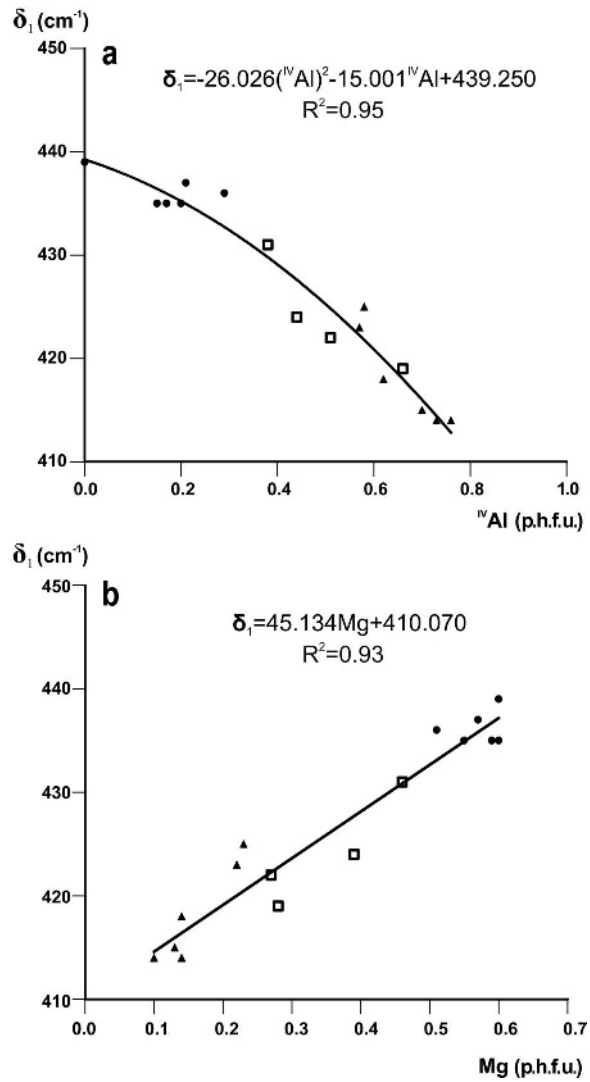


Figure 11. Band positions ($cm^{-1}$) of $\delta_1$ plotted *vs*. (a) $^{IV}$Al and (b) Mg contents (cations p.h.f.u.). Symbols as in Figure 4.

https://doi.org/10.1346/CCMN.2015.0630504 Published online by Cambridge University Press

Table 7. Tetrahedral Al, octahedral Mg, and octahedral Al cation contents (p.h.f.u.) in the samples studied as obtained from chemical analysis (c.a.) and calculated (calc.) using equations 4–6 (sample numbers as in Tables 1 and 2).

| # | Sample | $^{IV}$Al | | Mg | | $^{VI}$Al | |
|---|---|---|---|---|---|---|---|
| | | c.a. | calc. | c.a. | calc. | c.a. | calc. |
| 1 | RM30 | 0.73 | 0.74 | 0.14 | 0.09 | 1.86 | 1.91 |
| 4 | SG4 | 0.76 | 0.74 | 0.10 | 0.09 | 1.88 | 1.95 |
| 5 | RM35C | 0.70 | 0.72 | 0.13 | 0.11 | 1.82 | 1.88 |
| 6 | Fuzz-5 | 0.62 | 0.66 | 0.14 | 0.18 | 1.83 | 1.91 |
| 7 | Fuzz-6 | 0.58 | 0.51 | 0.23 | 0.33 | 1.75 | 1.60 |
| 8 | Zempleni | 0.57 | 0.55 | 0.22 | 0.28 | 1.78 | 1.74 |
| 9 | L-2A-1 | 0.66 | 0.64 | 0.28 | 0.20 | 1.57 | 1.53 |
| 11 | Swe-151 | 0.51 | 0.58 | 0.27 | 0.26 | 1.68 | 1.56 |
| 13 | IWi-1 | 0.44 | 0.53 | 0.39 | 0.31 | 1.44 | 1.42 |
| 15 | 60 | 0.38 | 0.34 | 0.46 | 0.46 | 1.32 | 1.32 |
| 16 | 602-1 | 0.29 | 0.17 | 0.51 | 0.57 | 1.39 | 1.35 |
| 17 | Z2 | 0.21 | 0.12 | 0.57 | 0.60 | 1.16 | 1.14 |
| 18 | 99-3/5 | 0.20 | 0.21 | 0.59 | 0.55 | 1.28 | 1.42 |
| 20 | Mal-4 | 0.17 | 0.21 | 0.55 | 0.55 | 1.34 | 1.35 |
| 21 | Mal-6 | 0.15 | 0.21 | 0.60 | 0.55 | 1.30 | 1.35 |
| 22 | 136 | 0 | 0.02 | 0.60 | 0.64 | 1.08 | 1.04 |

The $\delta_3$ mode is assigned to Si–O–Al bending vibration (octahedral Al) (Madejová, 2003). The shift of $\delta_3$ to lower wavenumbers in the transition from pyrophyllite to illite to aluminoceladonite may be associated with the increasing Si–O–Al angle as a result of increasing tetrahedral elongation in combination with increasing octahedral sheet thickness. Experimental structural data show that the tetrahedral elongation angle $O_{bas}$–T–$O_{ap}$ is 109.4º in pyrophyllite (Lee and Guggenheim, 1981), ~110–111º in muscovite (Rothbauer, 1971), ~112º in phengite (Ivaldi *et al.*, 2001), and ~113º in aluminoceladonite (Smyth *et al.*, 2000), while the octahedral sheet thickness simultaneously increases from 2.079 to 2.164 Å (Lee and Guggenheim, 1981, Zviagina and Drits, 2012). The increase in the Si–O–Al angle should reduce the vibration energy (Velde, 1978), so that the $\delta_3$ mode shifts to lower wavenumbers.

The position of $\delta_3$ in the illite–aluminoceladonite series is strongly correlated with $^{VI}$Al ($R^2$ = 0.93, Figure 13):

$$\delta_3 = 28.617\ ^{VI}Al + 479.28 \quad (6)$$

The octahedral Al cation contents can be estimated from equation 6 with an e.s.d. of 0.075 cations p.h.f.u. (Table 7).

*Al-O-Si in-plane vibration.* A well defined band at 753±3 $cm^{-1}$ is observed in the spectra of all illites irrespective of the amount of tetrahedral Al cations. In aluminoceladonites, the Al–O–Si in-plane vibration is either weak (for $^{IV}$Al = 0.15–0.29) or absent (samples 99-3/5 and 136 with $^{IV}$Al = 0.11 and 0, respectively) (Figure 2, Table 5).

*OH-stretching vibrations.* In both (Mg,Fe)-poor and Mg-rich illites, the OH-stretching region shows a wide absorption band resulting from superposition of individual cation-OH-cation vibrations, which can be identified from spectrum decomposition and curve-fitting (Figure 2a–c; Figure 3a,b). Besson and Drits (1997b) showed that in dioctahedral micas, the positions of the OH-stretching bands are determined by several competing factors. On the one hand, an increase in the total mass of cations bound to an OH group decreases the wavenumber. On the other hand, for cations having the same mass but different valences, two opposite trends interact. An increase in the total cation valence decreases the interaction within the OH group, but simultaneously increases the repulsion between the cations and the hydroxyl proton, thus weakening hydrogen bonds between OH and two apical oxygen anions in the octahedral sheet and strengthening the bond within the OH group. The latter effect dominates, and therefore an increase in the total cation valence increases the wavenumber. For the AlOHAl, AlOHMg, and MgOHMg stretching vibrations, the valence effect prevails over the mass effect, and therefore $\nu_{AlOHAl} > \nu_{AlOHMg} > \nu_{MgOHMg}$ (Besson and Drits, 1997b). Accordingly, in samples having 0.1–0.27 Mg cations p.h.f.u., the maximum absorption is determined by the AlOHAl vibration at 3627±3 $cm^{-1}$; in two samples with the Mg contents of ~0.4 cations p.h.f.u., 60 and IWi-1, the maximum is at 3606 and 3617 $cm^{-1}$, resulting from the AlOHMg vibration and the superposition of AlOHMg (3600 $cm^{-1}$) and AlOHAl (3621 $cm^{-1}$), respectively.

The OH-stretching region of the aluminoceladonite spectra differs dramatically from that of illites. The spectra of samples 136 (Figures 2d, 3c) and Z2 (not shown) consist of several sharp and well-resolved peaks; the other aluminoceladonites show a wide absorption band with one sharp maximum and poorly resolved peaks that can be identified from decomposition and curve-fitting (*e.g.* sample Mal-6, Figure 3d). As shown by Besson *et al.*

https://doi.org/10.1346/CCMN.2015.0630504 Published online by Cambridge University Press

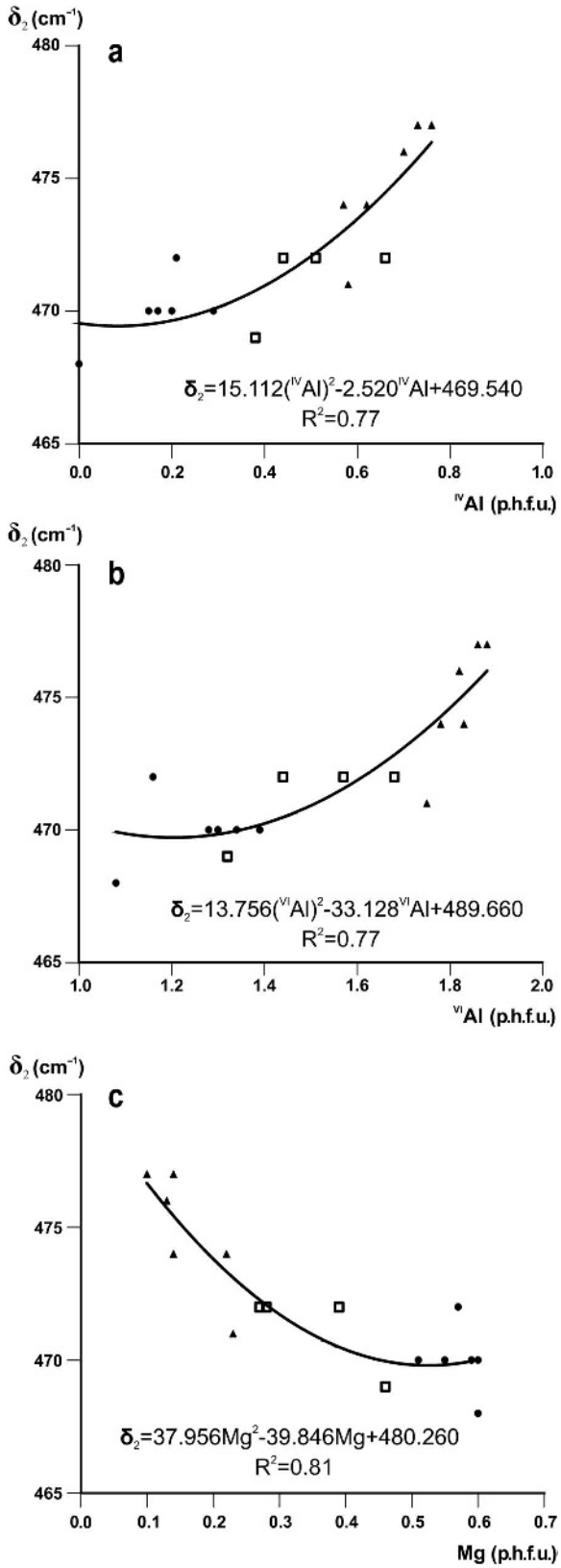


Figure 12. Band positions ($cm^{-1}$) of $\delta_2$ plotted *vs.* (a) $^{IV}$Al, (b) $^{VI}$Al, and (c) Mg contents (cations p.h.f.u.). Symbols as in Figure 4.

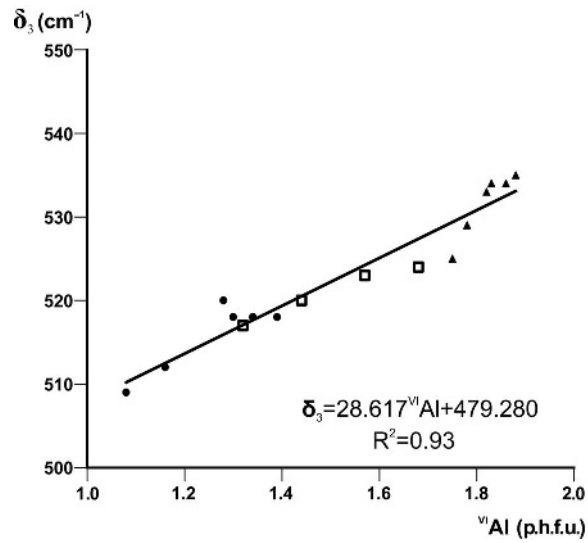


Figure 13. Band positions ($cm^{-1}$) of $\delta_3$ plotted *vs.* $^{VI}$Al contents (cations p.h.f.u.). Symbols as in Figure 4.

(1987) the resolution of the OH-stretching spectral region of dioctahedral 2:1 phyllosilicates, and aluminoceladonite in particular, is associated with the degree of order-disorder in the octahedral cation distribution. The typical feature of the aluminoceladonite spectra is the sharp maximum at ~3600 $cm^{-1}$, which corresponds to the AlOHMg stretching vibration. Another characteristic feature is the presence of the MgOHMg absorption band at 3583–3585 $cm^{-1}$, which can be identified either by visual inspection or, in the poorly resolved spectra, in the second derivative (Figure 3d).

The peculiarities of the OH-stretching region, in combination with the characteristic positions of the Si–O stretching and bending vibrations (Table 5) and the absence of the Al–O–Si in-plane vibration, can serve as identification criteria for aluminoceladonite. Distinguishing between Mg-poor and Mg-rich illites based solely on FTIR data appears problematic, but the position of the Si–O bending modes and the maximum absorption in the region of OH-stretching vibrations may serve as additional criteria.

## CONCLUSIONS

A detailed analysis of chemical and XRD data on a set of samples (Mg,Fe)-poor illite–Mg-rich illite–aluminoceladonite has shown that each group in the series is characterized by a unique combination of structural and crystal-chemical features. Composition ranges have been proposed and identification criteria have been formulated for each of the three mica groups (Table 6). Specifically, reduced values of $c\sin\beta$ (~9.9 Å) and $|c\cos\beta/a|$ (0.36–0.37) in combination with a relatively small $b$ parameter (9.00–9.02 Å) are clearly indicative of aluminoceladonite.

https://doi.org/10.1346/CCMN.2015.0630504 Published online by Cambridge University Press

Additional criteria for the identification of the mica varieties in the series have been provided based on a new approach to the interpretation of the FTIR spectra of illites and aluminoceladonites, which includes a set of relationships between tetrahedral and octahedral cation composition and positions of the Si–O bending and stretching modes. In particular, a sharp maximum at ~3600 $cm^{-1}$ and the presence of the MgOHMg stretching mode at 3583–3585 $cm^{-1}$, in combination with the specific band positions and profile of the Si–O bending and stretching region, are additional diagnostic features of aluminoceladonite.

The identification of the mica varieties in this series cannot be based solely on chemical analysis and should include structural data. In particular, high Mg contents in the crystal-chemical formula may indicate the presence of a Mg-rich smectite component (especially if combined with low K contents) or di-,trioctahedral domains resulting from the co-existence of *tv* and *cv* structure fragments (Drits *et al.*, 2010b), and not the presence of aluminoceladonite. The accurate evaluation of unit-cell parameters, which is essential for reliable identification, may present a non-trivial problem. Importantly, the samples studied should have a high degree of structural order to allow high-quality XRD patterns, so that reflection positions can be determined precisely and unit-cell parameters refined based on the experimental $d_{hkl}$ values. In the presence of a moderate amount of defects, such as stacking faults, the unit-cell parameters can be evaluated by the trial-and-error method based on the equations relating $d_{001}$, $d_{060}$, $d_{11\bar{2}}$, $d_{112}$, $d_{22\bar{1}}$, and $d_{\bar{1}31}$ to *a*, *b*, *c*, and β (Sakharov *et al.*, 1990; Drits *et al.*, 2010a). Simulation of the experimental XRD patterns from defective structures may also be efficient in the determination of unit-cell parameters (Sakharov *et al.*, 1990; Drits *et al.*, 2013). Finally, in the case of numerous stacking faults, analysis of XRD patterns from oriented preparations allows evaluation of the *c*sinβ value, an important characteristic for the identification of the mica varieties in the illite–aluminoceladonite series.

## ACKNOWLEDGMENTS

Thanks are due to Drs B. Sakharov, V. Krupskaya, and A. Derkowski for help and valuable comments, and Drs T. Ivanovskaya and V. Petrova for providing some of the samples. B. Zviagina, V. Drits, and O. Dorzhieva acknowledge the support of budget project #01201459179.

## REFERENCES

Bailey, S.W. (1984) Crystal chemistry of the true mica: Pp. 13–60 in: *Micas* (S.W. Bailey, editor). Reviews in Mineralogy, **13**. Mineralogical Society of America, Washington D.C.

Beran A., Voll, D., and Schneider, H. (2004) IR spectroscopy as a tool for the characterization of ceramic precursor phases. Pp. 189–226 in: *Spectroscopic Methods in Mineralogy* (A. Beran and E. Libowitzky, editors). EMU Notes in Mineralogy, **6**, Eötvös University Press, Budapest.

Besson, G. and Drits, V.A. (1997a) Refined relationships between chemical composition of dioctahedral fine-dispersed mica minerals and their infrared spectra in the OH stretching region. Part I. Identification of the stretching bands. *Clays and Clay Minerals*. **45**, 158–169.

Besson, G. and Drits, V.A. (1997b) Refined relationship between chemical composition of dioctahedral fine-dispersed mica minerals and their infrared spectra in the OH stretching region. Part II. The main factors affecting OH vibration and quantitative analysis. *Clays and Clay Minerals*, **45**, 170–183.

Besson, G., Drits, V.A., Dayniak, L.G., and Smoliar, B.B. (1987) Analysis of cation distribution in dioctahedral micaceous minerals on the basis of IR spectroscopy data. *Clays and Clay Minerals*, **22**, 465–478.

Beyer, S.R., Kyser, K., Hiatt, E.E., and Fraser, I. (2010) Geological evolution and exploration geochemistry of the Boomerang Lake unconformity-type uranium prospect, Northwest Territories, Canada. *Society of Economic Geologists*, *Special Publication*, **15**, 675–702.

Brigatti, M.F. and Guggenheim, S. (2002) Mica crystal chemistry and the influence of pressure, temperature and solid solution on atomistic models. Pp. 1–97 in: *Micas: Crystal Chemistry and Metamorphic Petrology* (A. Mottana, F.E. Sassi, J.B. Thompson Jr., and S. Guggenheim, editors). Reviews in Mineralogy and Geochemistry, **46**, Mineralogical Society of America, Washington, D.C. with Accademia Nazionale dei Lincei, Roma, Italy.

Drits, V.A. and Kossovskaya, A.G. (1991) *Clay Minerals: Micas and Chlorites*. Nauka, Moscow, 175 pp. (in Russian).

Drits, V.A. and McCarty, D.K. (2007) The nature of structure-bonded $H_2O$ in illite and leucophyllite from dehydration and dehydroxylation experiments. *Clays and Clay Minerals*, **55**, 45–58.

Drits, V.A., Weber, F., Salyn, A., and Tsipursky S.I. (1993) X-ray identification of 1*M* illite varieties. *Clays and Clay Minerals*, **28**, 185–207.

Drits, V.A., McCarty, D.K., and Zviagina, B.B. (2006) Crystal-chemical factors responsible for the distribution of octahedral cations over *trans*- and *cis*-sites in dioctahedral 2:1 layer silicates. *Clays and Clay Minerals*, **54**, 131–153.

Drits, V.A., Zviagina, B.B., McCarty, D.K., and Salyn, A.L. (2010a) Factors responsible for crystal-chemical variations in the solid solutions from illite to aluminoceladonite and from glauconite to celadonite. *American Mineralogist*, **95**, 348–361.

Drits, V.A., Ivanovskaya, T.A., Sakharov, B.A., Zviagina, B.B., Derkowski, A., Gor'kova, N.V., Pokrovskaya, E.V., Savichev, A.T., and Zaitseva, T.S. (2010b) Nature of the structural and crystal-chemical heterogeneity of the Mg-rich glauconite (Riphean, Anabar Uplift). *Lithology and Mineral Resources*, **45**, 555–576.

Drits, V.A., Sakharov, B.A., Ivanovskaya, T.A., and Pokrovskaya, E.V. (2013) Crystal-chemical microheterogeneity of Precambrian globular dioctahedral mica minerals. *Lithology and Mineral Resources*, **48**, 503–528.

Eberl, D.D., Środoń, J., Lee, M., Nadeau, P.H., and Northrop, H.R. (1987) Sericite from the Silverton Caldera, Colorado: Correlation among structure, composition, origin, and particle thickness. *American Mineralogist*, **72**, 914–934.

Farmer, V.C. (1974) The layer silicates. Pp. 331–363 in: *Infrared Spectra of Minerals* (V.C. Farmer, editor). Monograph **4**, Mineralogical Society, London.

Ferraris, G. and Ivaldi, G. (2002) Structural features of micas. Pp.117–153 in: *Micas: Crystal Chemistry and Metamorphic Petrology* (A. Mottana, F.E. Sassi, J.B. Thompson Jr., and S. Guggenheim, editors). Reviews in Mineralogy and Geochemistry, **46**. Mineralogy Society of America,

Washington, D.C. with Accademia Nazionale dei Lincei, Roma, Italy.

Grathoff, G.H., Moore, D.M., Kluessendorf, J., and Mikulic, D.G. (1995) The Waukesha illite, a Silurian residuum from karstification, proposed as a candidate for the Source Clay Repository. Program with abstracts, 32nd Annual Clay Minerals Society Meeting, Baltimore, Maryland, USA, p. 54.

Ivaldi, G., Ferraris, G., Curetti, N., and Compagnoni, R. (2001) Coexisting $3T$ and $2M_1$ polytypes in a phengite from Cima Pal (Val Savenca, western Alps): Chemical and polytypic zoning and structural characterization. *European Journal of Mineralogy*, **13**, 1025–1034.

Ivanovskaya, T.A., Tsipursky, S.I., and Yakovleva, O.V. (1989) Mineralogy of globular glauconites from Vendian and Riphean of the Ural and Siberia. *Litologia i Poleznye Iskopaemye*, **3**, 83–99 (in Russian).

Kardymowicz, I. (1960) O seladonicie z Barczy w Górach Swietokrzyskich. *Geological Quarterly*, **4**, 609–618.

Kloprogge, J.T., Frost, R.L., and Hickey, L. (1999) Infrared absorption and emission study of synthetic mica-montmorillonite in comparison to rectorite, beidellite and paragonite. *Journal of Materials Science Letters*, **18**, 1921–1923.

Lee, J.H. and Guggenheim, S. (1981) Single crystal X-ray refinement of pyrophyllite-1Tc. *American Mineralogist*, **66**, 350–357.

Madejová, J. (2003) FTIR techniques in clay mineral studies. *Vibrational Spectroscopy* **31**, 1–10.

Madejová, J. and Komadel, P. (2001) Baseline studies of the Clay Minerals Society Source Clays: infrared methods. *Clays and Clay Minerals*, **49**, 410–432.

Murao, R., Yubuta, K., Miyawaki R., and Sugiyama, K. (2009) Analysis of aluminoceladonite included in green heulandite. JAKOKA: 2009 Annual Meeting of the Japan Association of Mineralogical Sciences, abstract R4–11, p. 105.

Petrova, V.V. and Amarjargal, P. (1996) *Zeolites of Mongolia*, Nauka, Moscow, 150 pp. (in Russian).

Rasskazov, A.A. (1984) *Clay Minerals of Potassium-bearing Deposits* (area of Starobinsky deposit). Nauka, Moscow, 72 pp. (in Russian)

Rieder, M., Cavazzini, G., D'yakonov, Y.S., Frank-Kamenetskii, V.A., Gottardi, G., Guggenheim, S., Koval, P.V., Muller, G., Neiva, A.M.R., Radoslovich, E.W., Robert J.-L., Sassi, F.P., Takeda, H., Weiss, Z., and Wones, D.R. (1998) Nomenclature of the micas. *Clays and Clay Minerals*, **46**, 586–595.

Ripp, G.S., Doroshkevich, A.G., Karmanov, N.S., and Kanakin, S.V. (2009) Micas from the Khaluta carbonatite deposit, Western Transbaikal Region. *Geology of Ore Deposits*, **51**, 812–821.

Rothbauer, von, R. (1971) Untersuchung eines $2M_1$-muskovits mit neutronenstrahlen. *Neues Jahrbuch für Mineralogie Monatshefte*, 143–154.

Russell, J.D. and Fraser, A.R. (1994) Infrared methods. Pp. 11–67 in: *Clay Mineralogy: Spectroscopic and Chemical Determinative Methods* (M.J. Wilson, editor). Chapman & Hall, London.

Ryan, P.C., Coish, R., and Joseph, K. (2007) Ordovician K-bentonites in western Vermont: mineralogic, stratigraphic and geochemical evidence for their occurrence and tectonic significance. *Geological Society of America Abstracts with Programs*, **39**, no.1, p. 50.

Sakharov, B.A., Besson, G., Drits, V.A., Kameneva, M.Yu., Salyn, A.L., and Smoliar, B.B. (1990) X-ray study of the nature of stacking faults in the structure of glauconites. *Clay Minerals*, **25**, 419–435.

Schmidt, M.W., Dugnani, M., and Artioli, G. (2001) Synthesis and characterization of white micas in the join muscovite-aluminoceladonite. *American Mineralogist*, **86**, 555–565.

Seifert, F. (1968) X-ray powder data for Mg-A1-celadonite (leucophyllite) from Barcza, Poland. *Contributions to Mineralogy and Petrology*, **19**, 93–96.

Slonimskaya, M.V., Drits, V.A., Finko, V.I., and Salyn, A.L. (1978) The nature of interlayer water in fine-dispersed muscovites. *Izvestiya Akademii Nauk SSSR, Seriya Geologicheskaya*, **10**, 95–104 (in Russian).

Smyth, J.R., Jacobsen, S.D., Swope, R.J., Angel, R.J., Arlt, T., Domanik K., and Holloway, J.R. (2000) Crystal structures and compressibilities of synthetic $2M_1$ and $3T$ phengite micas. *European Journal of Mineralogy*, **12**, 955–963.

Sokolova, T.N., Drits, V.A., Sokolova, A.L., and Stepanov, S.S. (1976) Structural and mineralogical characteristics and conditions of formation of leucophyllite from salt-bearing deposits of Inder. *Litologia i Poleznye Iskopaemye*, **6**, 80–95 (in Russian).

Środoń, J. and Eberl, D.D. (1984) Illite. Pp. 495–544 in: *Micas* (S.W. Bailey, editor). Reviews in Mineralogy, **13**, Mineralogical Society of America, Washington D.C.

Środoń, J., Elsass, F., McHardy, W.J., and Morgan, D.J. (1992) Chemistry of illite-smectite inferred from TEM measurements of fundamental particles. *Clays and Clay Minerals*, **32**, 337–349.

Środoń, J., Clauer, N., Huff, W., Dudek, T., and Banaś, M. (2009a) K-Ar dating of the Lower Palaeozoic K-bentonites from the Baltic Basin and the Baltic Shield: implications for the role of temperature and time in the illitization of smectite. *Clay Minerals*, **44**, 361–387.

Środoń, J., Zeelmaekers, E., and Derkowski, A. (2009b) The charge of component layers of illite-smectite in bentonites and the nature of end-member illite. *Clays and Clay Minerals*, **57**, 649–671.

Środoń, J., Paszkowski, M., Drygant, D., Anczkiewicz, A., and Banas, M. (2013) Thermal history of Lower Paleozoic rocks on the Peri-Tornquist margin of the East European Craton (Podolia, Ukraine) inferred from combined XRD, K-Ar, and AFT data. *Clays and Clay Minerals*, **61**, 107–132.

Velde, B. (1978) Infrared spectra of synthetic micas in the series muscovite-MgAl celadonite. *American Mineralogist*, **63**, 343–349.

Velde, B. (1980) Cell dimensions, polymorph type, and infrared spectra of synthetic white micas: the importance of ordering. *American Mineralogist*, **65**, 1277–1282.

Viczián, I. (1997) Hungarian investigations on the "Zempleni" illite. *Clays and Clay Minerals*, **45**, 114–115.

Wilson, M.J. (2013) *Rock-Forming Minerals, Volume 3C, Sheet Silicates: Clay Minerals* (by W.A. Deer, R.A. Howie, and J. Zussman). The Geological Society, London, 724 pp.

Zviagina, B.B. and Drits, V.A. (2012) Structural regularities in $2M_1$ dioctahedral micas: The structure modeling approach. *American Mineralogist*, **97**, 1939–1954.

Zviagina, B.B., McCarty, D.K., Środoń, J., and Drits V.A. (2004) Interpretation of infrared spectra of dioctahedral smectites in the region of OH-stretching vibrations. *Clays and Clay Minerals*, **52**, 399–410.

Zviagina, B.B., Sakharov, B.A., and Drits V.A. (2007) X-ray diffraction criteria for the identification of *trans*- and *cis*-vacant varieties of dioctahedral micas. *Clays and Clay Minerals*, **55**, 467–480.

(*Received 3 June 2015; revised 17 November 2015; Ms. 1008; AE: W.D. Huff*)